Interaction Dynamics of a Spherical Particle with a Suspended Liquid Film

Subhasish Mitra, Elham Doroodchi, and Geoffrey M. Evans
Discipline of Chemical Engineering, School of Engineering, University of Newcastle, Callaghan, NSW 2308 Australia

Vishnu Pareek
Dept. of Chemical Engineering, Curtin University, Perth, WA 6102, Australia

Jyeshtharaj B. Joshi
Dept. of Chemical Engineering, Homi Bhabha National Institute, Anushaktinagar, Mumbai 400 094, Maharashtra India

DOI 10.1002/aic.15027
Published online September 21, 2015 in Wiley Online Library (wileyonlinelibrary.com)

Hydrodynamics of collision interactions between a particle and gas-liquid interface such as droplet/film is of keen interest in many engineering applications. The collision interaction between a suspended liquid (water) film of thickness 3.41 ± 0.04 mm and an impacting hydrophilic particle (glass ballotini) of different diameters (1.1–3.0 mm) in low particle impact Weber number ($We = \rho_l v_p^2 d_p/\sigma$) range (1.4–33) is reported. Two distinct outcomes were observed—particle retention in the film at lower Weber number and complete penetration of the film toward higher Weber number cases. A collision parameter was defined based on energy balance approach to demarcate these two interaction regimes which agreed reasonably well with the experimental outcomes. It was shown that the liquid ligament forming in the complete penetration cases breaks up purely by "dripping/end pinch-off" mechanism and not due to capillary wave instability. An analytical model based on energy balance approach was proposed to determine the liquid mass entrainment associated with the ligament which compared well with the experimental measurements. A good correlation between the %film mass entrained and the particle Bond number ($Bo = \rho_l g d_p^2/\sigma$) was obtained which indicated a dependency of $Bo^{1.72}$. Computationally, a three-dimensional CFD model was developed to simulate these interactions using different contact angle boundary conditions which in general showed reasonable agreement with experiment but also indicated deficiency of a constant contact angle value to depict the interaction physics in entirety. The computed force profiles from computational fluid dynamics (CFD) model suggest dominance of the pressure force over the viscous force almost by an order of magnitude in all the Weber number cases studied. © 2015 American Institute of Chemical Engineers *AIChE J*, 62: 295–314, 2016

Keywords: particle-film collision, interface, ligament, end pinching-off, liquid entrainment, CFD

Introduction

In-depth understanding of collision interaction of particles with gas-liquid interface is the key to successful design and optimization of many process engineering applications. Some of these applications include but not limited to coating of particles; scrubbing of dust-laden off gases; mixing of feed droplets and catalyst particles in the vaporization zone of fluidized catalytic cracking reactors;[1–3] fluid coking of bitumen, spray drying,[4] fabrication of ceramic reinforced metal composites,[5] recovery of valuable minerals by film flotation process,[6] and many more.

In all of these interactions involving multiple interfaces, two distinct geometry of gas-liquid interface can be identified—planar interface and curved interface. Depending on the geometry of interface and impacting particle, different interaction outcomes are observed. A significant number of studies are available on the interactions of cylindrical[7] and spherical[8–10] objects on a large planar interface reporting phenomena like floating, sinking, and rebounding. These studies focused on explaining the load carrying capacity of liquid under different combinations of solid surface hydrophobicity and physical properties of liquid citing relevance to biological instances like insects walking on water.[8] Among other applications, recovery of valuable mineral particles from gangue materials is also reported utilizing the suitable interactions of hydrophilic particles with planar gas-liquid interface in film floatation process.[6]

However, relatively fewer studies are indeed reported on interaction of a particle with a curved interface, that is, droplet which include applications like feed droplet vaporization in contact with hot catalyst particles in fluid catalytic cracking (FCC) unit,[1–3] interactions of fine particles from recycled exhaust stream with feed droplets in spray drying system,[4] and

Additional Supporting Information may be found in the online version of this article.

Correspondence concerning this article should be addressed to G. M. Evans at Geoffrey.Evans@newcastle.edu.au

© 2015 American Institute of Chemical Engineers

penetration behavior of ceramic particulates into molten aluminum droplet in light weight metal matrix fabrication system.[5]

Although many complex collision interactions are possible between a pair of particle and droplet, the three most general interaction types based on the size ratio could be summarized as follow: (A) a small droplet and larger particle; (B) a pair of droplet-particle of nearly unity size ratio; and (C) a small particle and larger droplet.

For interaction type A, largely three different outcome modes can be observed: (1) sticking or deposition of droplet on particle, (2) rebound of droplet from particle surface, and (3) splashing (disintegration) of droplet after impact. Central to such dynamics is the interplay between inertia, surface tension force, and viscous force which are quantified using dimensionless groups such as Weber number ($We = \rho_l v^2 d/\sigma_{lg}$) Reynolds number ($Re = dv\rho_l/\mu_l$), Ohnesorge number ($Oh = \mu_l/\sqrt{\rho_l \sigma_{lg} d}$), and Capillary number ($Ca = \mu_l v/\sigma_{lg}$)[1,2,10] where d is droplet diameter, v is relative velocity between interacting droplet and particle, and ρ_l, μ_l, and σ_{lg} are liquid density, viscosity, and surface tension, respectively. At lower Weber number, surface tension force dominates over inertia which results in deposition of droplet on particle surface. When the particle surface is hydrophobic (low energy surface), such interactions result in rebound of the impacting droplet due to restoring surface tension force. In relatively higher inertia impact, resistance due to both surface tension and viscous force is surpassed yielding into disintegration of the droplet into many secondary droplets.

In Type B interaction, three distinct outcome modes are reported as a function of collision angle (impact parameter) and Weber number. In a recent study, various types of possible outcomes from Type B interactions between a pair of droplet and particle of the order of unity size ratio were demonstrated using Lattice-Boltzmann simulation method.[11] In the increasing order of Weber number, the outcomes in this particular case can be summarized as: (1) deposition or coalescence (droplet spreads over particle as a thin film), (2) ripping and coating (some part of droplet remains deposited on particle while the other part forms a secondary droplet), and (3) skirt scattering (a conical/skirt type ligament forms which subsequently breaks into many secondary droplets).

Type C interaction, on the other hand, remains much less investigated and from the very few experimental studies available,[3,12] the following four different outcome modes are known: (1) particle rebounds off the interface, (2) partial penetration of particle at gas-liquid interface with oscillatory motion, (3) capture/retention (complete penetration of particle at gas-liquid interface but no exit from the liquid-gas side interface), and (4) complete penetration of particle through both interfaces (gas-liquid and liquid-gas).

The first three modes in Type C interactions invariably occur in the low Weber number regime while the fourth mode specifically occurs in the high Weber number regime. In mode (1), rebound event is usually observed when a superhydrophobic particle (contact angle $>150°$) impacts on a low viscous liquid with density higher than the particle. This is due to the fact that component of the capillary force arising due to deformation of the interface works in the opposite direction of particle motion and can balance the inertia of the impacting particle. This phenomenon leads to floating of solid objects denser than water. Vella et al.,[8] showed that maximum density of an impacting particle increases with increase in the contact angle, that is, hydrophobicity of the particle surface. In a later work, Lee and Kim[10] experimentally showed that superhydrophobic particles (radius: 0.67–1 mm) of different density ratio (particle density/water density: 0.88–2.48) during impact on an air-water interface at different impact velocity can exhibit distinct impact behavior, that is, damped oscillation (impact velocity: 1.23 m/s), complete bouncing-off (impact velocity: 1.84 m/s), and sinking through interface (impact velocity: 1.93 m/s). They, however, reported that this rebounding behavior disappears as the viscosity of the liquid phase is gradually increased.

Modes (2) and (3) represent the outcome of particle capture/retention, whereby particle inertia is completely dissipated to overcome the various resistive forces experienced in the droplet body. Due to formation and subsequent breakup of the concave gas cavity in mode (3), a bubble may get entrained along with particle. Mode (4) refers to outcome of complete penetration where particle has sufficient inertia to overcome all the resistances in droplet. Similar to mode (3), mode (4) may also exhibit entrainment of a bubble attached to particle surface. Also, when the impact inertia of particle is very high and droplet is less viscous, the primary target droplet may be completely disintegrated into multiple secondary droplets upon impact.[12] Another interesting characteristic observed in interaction mode (4), is the entrainment of liquid mass being attached to impacting particle surface.[11,12]

Quantification of the entrained liquid mass is often important for collision-induced heat and mass transport processes. Dubrovsky et al.[12] quantified the entrained liquid mass in their study empirically by correlating it with the dimensionless numbers without actually addressing the mechanism of this physical process. Using Lattice Boltzmann method (LBM) simulation technique, Gac and Gradon[11] demonstrated such attachment behavior of liquid mass to particle surface during high relative velocity interaction cases, however, the entrained mass was not quantified.

We have previously investigated interaction of a small particle with a larger stationary droplet supported on a solid surface using high speed imaging and three-dimensional (3-D) CFD modeling.[3] While the earlier studied system was useful for observing/quantifying the interactions modes (2) and (3) described earlier, it could not be used to study interaction mode (4) where complete penetration of the colliding particle through the droplet is expected. To explore mode (4) interaction, ideally the system should comprise a freely moving particle and a droplet in a controlled interaction environment. Presumably, however quantifying particle trajectory inside the droplet experimentally in this case would be very challenging. Consequently in this study, the moving droplet was replaced by a fixed horizontally suspended liquid film of dimensions comparable to the impacting particle in a capillary tube. The system was considered ideal to observe the interaction behavior of a vertically impacting solid particle with the suspended film mimicking a stationary droplet with both interfaces (gas-liquid and liquid-gas) available for interaction.

Specifically, the present system was investigated to: (1) experimentally determine the different interaction outcomes at varying Weber numbers and also determine particle trajectory in the film, (2) quantify a collision parameter to predict the interaction outcomes based on an energy balance approach, (3) suggest a mechanism for liquid entrainment with particle during complete penetration, (4) quantity the liquid mass entrainment with particle based on the energy balance approach developed in (2) and (5) simulate experimentally observed interaction outcomes and particle trajectory in the

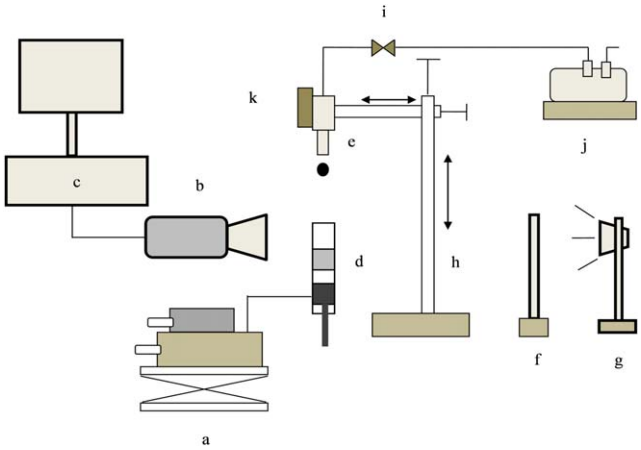

Figure 1. Schematic of experimental setup—(a) X-Y optical traverse with height elevation jack, (b) high speed CCD camera, (c) computer, (d) capillary tube holding the liquid film with a piston at bottom, (e) particle release nozzle, (f) diffuser screen, (g) light source, (h) particle release nozzle position varying mechanism, (i) solenoid valve, (j) vacuum pump, and (k) laser source for alignment purpose.

[Color figure can be viewed in the online issue, which is available at wileyonlinelibrary.com.]

film using a 3-D CFD model developed based on multiphase volume of fluid (VOF) method combined with the dynamic meshing algorithm and quantify contribution of the associated forces during collision.

The rest of the article is organized as follows: first the experimental work and quantification of experimental data using image processing technique are discussed; then a model based on energy balance approach is introduced to quantify interactions outcomes and liquid mass entrainment with particle; next the CFD modeling methodology in presented followed by results and discussions and summary of findings at the end.

Experimental

Methodology

An experimental apparatus was designed to perform controlled experiments to study particle-film collision interactions (Figure 1). Glass ballotini particles (Potter Mix, Australia) of different sizes in the range of 1.1–3.0 mm were used. A liquid film of pure water (RO filtered) was formed manually inside a transparent polypropylene capillary tube (d) of inner diameter 4.61 mm using a 1-mL syringe. The tube was thoroughly cleaned with soap solution and acetone to remove any dirt and dried every time using compressed air before forming the film. To determine the film mass, the capillary tube was weighed before and after film formation. The measured film mass was ensured to remain within a narrow band of deviation from a mean value after several repeated measurements leading to a consistent film thickness of 3.41 ± 0.04 mm where "$\pm$" indicates one standard error. As capillary force alone was not sufficient by itself to support the liquid film of such mass, gradual descent of the film down the tube was prevented by applying an upward pressure using a tightly sealed piston at the bottom of capillary tube. The tube assembly was mounted on an X-Y optical traverse with micrometric precision.

A particle release mechanism (h) capable of sliding both in horizontal and vertical directions with millimetric precision was used to hold the particle at the tip of a stainless steel capillary nozzle (ID 0.03″) by vacuum. A vacuum pump (j) was connected to the nozzle via a solenoid valve (i). The particle release process was triggered by breaking the vacuum pull when the solenoid valve was turned off.

To ensure that particle fall was consistent, a separate experiment was carried out by dropping the particle several times from the same position. A normal distribution of particle centroid was obtained with insignificant standard deviation in particle velocity in downward direction which confirmed the consistency of particle trajectory. A low power (<5 mW) laser source (k) was aligned in parallel with the particle release nozzle. This arrangement assisted in alignment of particle release nozzle with capillary tube below by ensuring that laser beam always pointed toward the center of the capillary tube before the particle was dropped.

The impact velocity of the particle was varied in the experiment by changing the position of the particle release nozzle in the vertical direction. In those cases where the particle completely penetrated the liquid film and settled at bottom of the tube, the remaining film above was carefully absorbed in a cotton wick. Mass of liquid adhered to the particle surface was then determined by measuring mass difference of the capillary tube before and after collision using a precision weighing balance where the particle mass was known by prior measurement. Each experiment for each size range of particle was repeated at least five times for five different impact velocities.

Contact angles of the capillary tube and the glass particles were measured in separate experiments. For the capillary tube, static contact angle,θ_t was measured by Jurin's principle by measuring the liquid height depression, h_t from the images from the well-known expression $h_t = \frac{4\sigma_{lg}\cos\theta_t}{(\rho_l - \rho_g)gd_t}$ where ρ_l, ρ_g is liquid and gas density, σ_{lg} is surface tension, g is gravitational constant, and d_t is insider diameter of the capillary tube.

To measure contact angles on the glass particle, a thoroughly cleaned 5-mm diameter particle attached to a glass slide was used. Static contact angle was measured by depositing a single drop of RO water axisymmetrically using a precision syringe pump on the particle. To determine the advancing and receding contact angles, the principle of inclined/tilted plane was followed. Using a precision syringe pump, liquid was continually injected at a rate of 5 μL/min to a sessile droplet placed symmetrically on the top of the particle until the droplet grow big enough to commence rolling over the particle surface. The advancing contact angle was measured at the moving front of the droplet and the receding contact angle was measured at the trailing end. The experiments were performed at least five times and a range of advancing and receding contact angles were obtained. All the measured contact angles are provided in Table 1.

A backlighting imaging technique was used obtain good contrast images in shadowgraphy mode by placing a diffuser screen in front of a halogen light source (12 V, 50 W). The interaction dynamics of particle with film was captured by a high speed complementary metal oxide semiconductor (CMOS) sensor camera (Phantom v311, Vision Research) at 1953 frame per second and 35 μs exposure time in a field of view of 512×800 pixels yielding a resolution of 24.5 μm/pixel.

Image processing

Image processing was carried out to determine particle positions from the images taken at different time instances. The

Table 1. Contact Angle Values for Air/Water/Glass Particle System and Air/Water/Polypropylene Capillary Tube System

System/Cases	Measured at Thermodynamic Equilibrium			Measured at Unsteady State	
	Advancing Contact Angle (Static)	Receding Contact Angle (Static)	Static Contact Angle	Advancing Contact Angle (Dynamic) (Eq. 10b)	Advancing Contact Angle (Dynamic)
Air/water/glass particle	56–75°	22–43°	47–58°	–	–
Air/water/PP tube			105 ± 2°		–
We-1.4				87°	
We-11.7				98°	110 ± 10°
We-22.5				102°	110 ± 10°

particle boundary was tracked based on the difference in pixel intensity relative to the background. Due to some inconsistency in pixel intensity in captured images, first the pixel counts over the grayscale values (0–256) were made uniform by manipulating the image histogram. Figure 2 presents the distribution of pixel counts in the image over the entire grayscale range before and after the image processing. It can be seen that pixel counts becomes more uniform after image processing. Next, the sharpness of the images was improved and edges/boundaries were determined. A circle was then fitted (Figure 2) to the marked boundary based on the pixel intensity difference on the boundary and background using an appropriate range of search radius. Data of equivalent spherical radius and centroids were then obtained which were used in the all subsequent calculations related to particle motion.

A similar boundary profile marking technique was applied to determine the contact angle on particle surface. To do this, first the center point of the particle was found out by fitting a circle to the marked particle boundary. The intersection points of the drop interface on the particle surface were then determined and connected to center point. Tangents were then drawn to at the intersection points to determine the contact angle. All particle image processing was performed using both an in-house *MATLAB* (*ver: R2012b*) code and *Image J* (NIH) software.

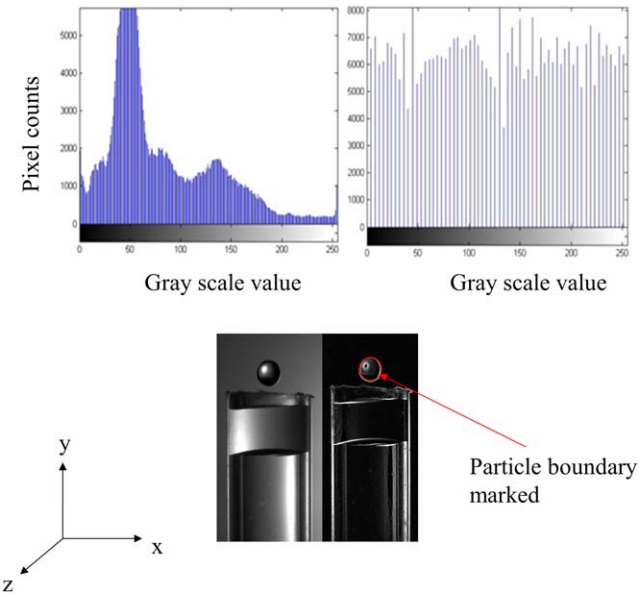

Figure 2. Image processing showing pixel intensity distribution of raw image before and after image processing.

Uniform pixel intensity distribution is obtained after processing. The particle boundary is marked and a circle is fitted to compute centroid and diameter. [Color figure can be viewed in the online issue, which is available at wileyonlinelibrary.com.]

Mathematical Modeling

In this section, a modeling approach is presented based on energy balance of the particle-film system to define a collision parameter for predicting two major collision outcomes—retention/capture and complete penetration. Also, the energy balance approach is used to quantify liquid mass entrainment with particle during complete penetration.

Energy balance of particle-film system

Figure 3a illustrates the initial energy of the particle-film system at $t = t_0$ when a particle of diameter d_p and density ρ_p is just about to touch the film interface (position A), and final energy of the system at $t = t_f$ when particle possesses enough energy to entrain a liquid mass enclosed in a conical-shaped liquid ligament (position B). It was assumed that the system comprising particle, film, and gas above and below film interface behaves adiabatically (all heat energy terms being zero). Therefore, change in energy of the system before and after particle impact could be expressed following the first law of thermodynamics as

$$\Delta E_{AB} = -W \tag{1}$$

where ΔE_{AB} is the energy change of the system between positions (A) and (B) and W represent all the works terms. The negative sign in the work term in Eq. 1 indicates that work done by the system is due to the loss of kinetic energy of the particle.

The energy change of the system comprises change in the energy of particle (ΔE_p), change in the energy of film (ΔE_f), and change in the energy of surrounding gas (ΔE_g) above and below film interface which can be expressed as

$$\Delta E_{AB} = \Delta E_p + \Delta E_f + \Delta E_g \tag{2}$$

The particle was released from rest at a certain height from the top gas-liquid interface (not shown) so that when it reaches position (A) at the top interface, potential energy is converted to the kinetic energy. In the complete penetration case, at position (B), particle attaches itself to some entrained mass of liquid and still possesses some residual kinetic energy. Also, the surface energy of the particle changes as the particle descends into the liquid phase (solid-liquid interface) from the gas phase (solid-gas interface) above. Change in the particle surface

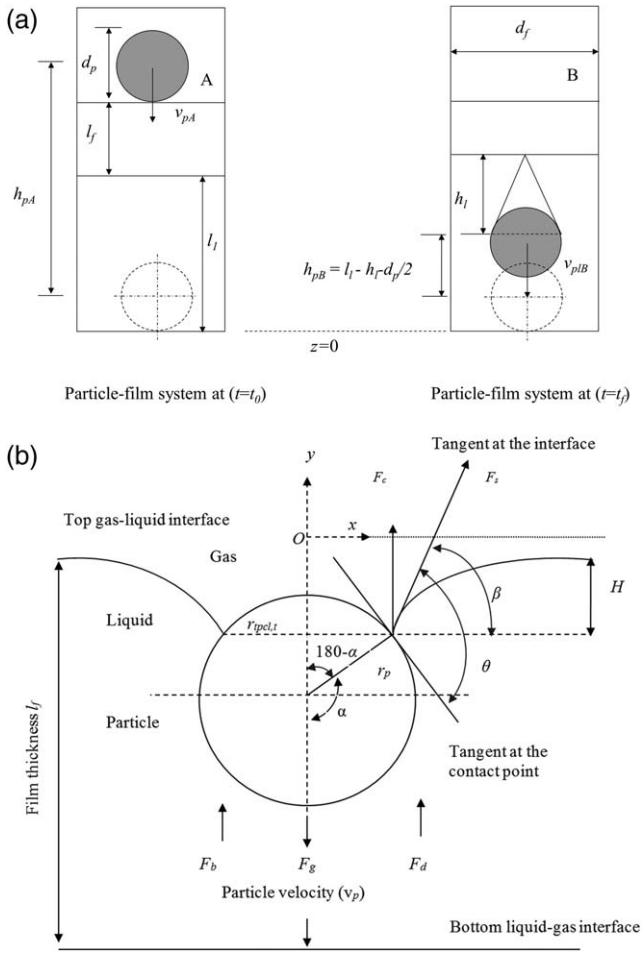

Figure 3. Schematic of (a) particle-film system before impact ($t = t_0$) and after impact ($t = t_f$) and (b) top interface depression during penetration event and associated forces in the liquid film opposing particle motion.

energy, kinetic energy, and potential energy at positions (A) and (B) therefore can be expressed as

$$\Delta E_{\mathrm{p}} = \left[S_{\mathrm{pA}} + \frac{1}{2}\left(\frac{\pi d_{\mathrm{p}}^3 \rho_{\mathrm{p}}}{6}\right) v_{\mathrm{pA}}^2 + \left(\frac{\pi d_{\mathrm{p}}^3 \rho_{\mathrm{p}}}{6}\right) g h_{\mathrm{pA}} \right]_{\mathrm{A}} - \left[S_{\mathrm{pB}} + \frac{1}{2}\left(\frac{\pi d_{\mathrm{p}}^3 \rho_{\mathrm{p}}}{6} + m_{\mathrm{l}}\right) v_{\mathrm{plB}}^2 + \left(\frac{\pi d_{\mathrm{p}}^3 \rho_{\mathrm{p}}}{6} + m_{\mathrm{l}}\right) g h_{\mathrm{pB}} \right]_{\mathrm{B}} \tag{3}$$

where S_{pA} and S_{pB} are particle surface energy at positions A and B, m_{l} is liquid mass, v_{pA} is particle velocity at position A, v_{plB} is combined particle-ligament velocity at position B, and h_{pA}, h_{pB} are heights of particle center of gravity from datum level ($z = 0$) before and after impact, respectively. Referring to Figure 3a, height h_{pA} was obtained by adding the film thickness (l_{f}) and distance of bottom film interface (l_{l}) from datum level ($z = 0$) and h_{pB} was obtained by subtracting length of liquid ligament (h_{l}) and particle radius ($d_{\mathrm{p}}/2$) from l_{l}.

The solid-gas interfacial energy of the particle surface (S_{pA}) before impact (at position A) can be expressed as

$$S_{\mathrm{pA}} = \pi d_{\mathrm{p}}^2 \sigma_{\mathrm{sg}} \tag{4a}$$

where σ_{sg} is the solid-gas surface tension of glass particle.

Following the penetration of the film at position B where the particle is covered by a thin liquid layer, the liquid-solid surface energy can be given as

$$S_{\mathrm{pB}} = \pi d_{\mathrm{p}}^2 \sigma_{\mathrm{sl}}, \tag{4b}$$

While it is indeed difficult to obtain the interfacial energy individually from Eqs. 4a and 4b, their difference could be readily determined from the well-known Young equation if the static contact angle data on the solid surface is available. Using this equilibrium relationship: $\sigma_{\mathrm{sg}} - \sigma_{\mathrm{sl}} = \sigma_{\mathrm{lg}} \cos\theta_{\mathrm{s}}$, the difference in surface energy due to wetting can be expressed as

$$S_{\mathrm{pA}} - S_{\mathrm{pB}} = \pi d_{\mathrm{p}}^2 \sigma_{\mathrm{lg}} \cos\theta_{\mathrm{s}} \tag{4c}$$

where σ_{lg} is liquid-gas surface tension and θ_{s} is the static contact angle of liquid on solid surface.

Due to curved nature of film interface in the capillary tube, the vertical capillary force components at top and bottom interface cancel each other and the film descends downward by its own gravity force. To make the film stationary, an upward positive pressure was applied (~30 Pa) just enough to support the film weight which nullifies the effect of gravity. The only potential energy the film has therefore is surface energy stored at the interfaces. Evaporation from liquid interfaces was neglected to keep validity of the adiabatic assumption. Although some motion is imparted into the film by the impinging particle, its displacement was not found to be significant in the experiment. This was confirmed by analyzing the images before and after the particle impact where the displacement of both top and bottom interface of the film was found to be less than 0.4 mm. For this reason, any variation in the contact angle of water on the capillary tube was not included in the analysis on purpose to keep it simple. After impact, a nearly conical-shaped ligament of length h_{l} is created at the expense of particle kinetic energy at position (B). Accounting for this new surface area, change in entire film energy therefore could be given as

$$\Delta E_{\mathrm{f}} = \left[S_{\mathrm{fA}} \sigma_{\mathrm{lg}} \cos\theta_t - \left(S_{\mathrm{fB}} \sigma_{\mathrm{lg}} \cos\theta_t + S_{\mathrm{lig}} \sigma_{\mathrm{lg}} \right) \right] \tag{4d}$$

where S_{fA} and S_{fB} are surface area of film at positions A and B, θ_t is the static contact angle of water on the capillary tube wall, and S_{lig} is surface area of the ligament at position B.

The measured static contact angle of water on the capillary tube, θ_t was obtained as $105 \pm 2^\circ$ (Table 1).

Before impact, particle imparts some motion to the surrounding gas which increases kinetic energy of gas and after impact at position (A), the top wavy interface also passes on some kinetic energy to the surrounding gas. During impact, complex interface undulations occur which leads to change in the system volume and corresponding change in the gas pressure. These effects, however, were difficult to quantify in the present modeling framework and subsequently neglected in the gas-phase energy balance which led to

$$\Delta E_{\mathrm{g}} = 0 \tag{5}$$

It will be shown later in the analysis of forces using CFD model that static pressure magnitude at the instance of ligament breakup (position B) remains almost unaltered which justifies this assumption.

Now, incorporating all the energy change terms from Eqs. 3–5 into Eq. 1, the complete energy balance of the system could be obtained as

$$\left[\pi d_p^2\sigma_{lg}\cos\theta_s+\frac{1}{2}\left(\frac{\pi d_p^3\rho_p}{6}\right)v_{pA}^2+\left(\frac{\pi d_p^3\rho_p}{6}\right)gh_1+S_{fA}\sigma_{lg}\cos\theta_t\right]_A-$$
$$\left[\frac{1}{2}\left(\frac{\pi d_p^3\rho_p}{6}+m_l\right)v_{plB}^2+\left(\frac{\pi d_p^3\rho_p}{6}+m_l\right)gh_2+S_{fB}\sigma_{lg}\cos\theta_t+S_{lig}\sigma_{lg}\right]_B=-W. \quad (6)$$

Work terms (W)

During penetration of the film, particle spends its kinetic energy by performing work against various opposing forces such as buoyancy, drag, and capillary force. A detailed schematic of the particle-film interaction process[3,6,13] at the top interface indicating the geometry and forces is shown in Figure 3b. The interface deforms as the particle moves downward and a three phase contact line (TPCL) of radius, r_{tpcl}, forms on the particle surface. The interface inclination angle during deformation is denoted by β while the submergence of the particle is denoted by the penetration angle, α, which varies from 0 to 180° denoting zero to complete penetration. Contact angle, θ is obtained by drawing two tangents at the interface and at point of contact on particle surface, respectively. Note that the penetration angle, α, from geometric consideration, can also be obtained by subtracting β from θ. The different work terms are described below.

Buoyancy

While traveling through the film, particle experiences an upward buoyancy force due to hydrostatic pressure difference at its bottom and top surface. Energy spent to overcome the resistance of the buoyancy can be obtained by integrating the buoyancy force over the film thickness, l_f as

$$E_b=\int_0^{l_f}\frac{\pi d_p^3\rho_l g}{6}dy \quad (7)$$

Fluid drag

Using the usual definition of drag force, energy spent by particle to overcome drag force across the film thickness, l_f can be calculated as

$$E_d=\int_0^{l_f}C_d\left(\frac{\pi d_p^2}{4}\right)\left(\frac{\rho_l v_{pA}^2}{2}\right)dy \quad (8)$$

where the below expressions of drag coefficient, C_d, were used for a particle immersing in liquid as suggested by Wu et al.[5]:

For $0<Re\leq 1$, $C_d=24/Re$

For $1<Re\leq 400$, $C_d=24/Re^{0.646}$

For $400<Re\leq 3\times 10^5$, $C_d=0.5$.

Capillary effect

At the state of partial submergence into interface, a TPCL forms on the particle surface. From Figure 3b, it can be noticed that surface tension force, F_s acts in the tangential direction along the curved interface and vertical component of F_s working on TPCL inhibits the downward motion of particle. For a three-phase system, this force is known as capillary force, F_c which remains active as long as the interface is attached to solid surface and becomes zero when the particle is completely immersed into the film (zero TPCL radius). The capillary force resists motion of particle as it passes through interfaces. From Figure 3b, it can be seen that the radius of TPCL can be given by $r_{tpcl}=r_p\sin(\alpha)$. Considering the vertical component of surface tension force, F_s on the TPCL, the capillary force can be expressed as[3,4,13]

$$F_c=2\pi r_p\sigma_{lg}\sin\alpha\sin\beta=2\pi r_p\sigma_{lg}\sin\alpha\sin(\theta-\alpha) \quad (9)$$

The interface penetration process involves dynamic change of contact angle subtended at the particle surface. It is noted that during penetration of the top interface of the film, a gas cavity forms over the submerging particle which is stretched as the particle descends further into the liquid eventually leading to snapping of the cavity at the narrowing necking point. An advancing contact angle is exhibited at this state, however, during penetration of the bottom interface, specifically in the higher Weber number cases; a receding contact angle is exhibited on the particle surface. The required energy, $E_{c,tf}$ to overcome the capillary force at the top interface can be derived by replacing θ with advancing contact angle, θ_a in Eq. 9 followed by differentiating the expression of F_c and then performing integration within the limit of penetration angle, α varying from 0 to $\pi/2$ as follows

$$E_{c,tf}=2r_p\int dF_c=2r_p\int_0^{\pi/2}2\pi r_p\sigma_{lg}\sin(\theta_a-2\alpha)d\alpha=4\pi r_p^2\sigma_{lg}\cos\theta_a\pi/2. \quad (10a)$$

In determining the work term from Eq. 10a, integration limit was set to $\pi/2$ to account for the maximum capillary work noting the fact that the capillary force expression given in Eq. (9) has maxima or minima at penetration angle $\alpha=/2$ for a given contact angle, θ. The capillary force thus obtained was considered to be active over the entire submergence distance (particle diameter, d_p) to yield the maximum work done. The actual energy spent against the capillary force in the entire duration of submergence however can be determined as $\int_0^{\pi}F_c dx=\frac{4}{3}\pi r_p^2\sigma_{lg}\cos\theta$ by setting the differential submergence distance, $dx=r_p\sin\alpha\, d\alpha$ which can be readily shown from Fig. 3. Determining an appropriate value for the dynamic contact angle in Eq. 10a is a challenging problem which depends on number of parameters such as roughness and chemical homogeneity of the solid surface and most importantly TPCL velocity. Formulation of the dynamic contact angle as a function of contact line velocity is a well-known complex problem due to the apparently "no-slip" condition on the solid surface. This problem has attracted considerable research attention and in general is resolved by considering molecular-hydrodynamic nature of the contact angle which allows contact line "slip" on the solid surface only in the molecular regime.[6,14] In this study, the dynamic advancing contact angle, θ_a in Eq. 10a was computed using the molecular-hydrodynamic model suggested by Petrov and Petrov[14] as follows

$$\theta_a=\sqrt[3]{\left\{\cos^{-1}\left[\cos\theta_s-\left(\frac{2kT}{\sigma_{lg}\lambda^2}\right)\sinh^{-1}\left(\frac{v_{tpcl}}{2K_w\lambda}\right)\right]\right\}^3+9Ca\ln\left(\frac{L_{cap}}{L_s}\right)} \quad (10b)$$

where θ_s is the static contact angle, k is Boltzmann constant, T is temperature, K_w is a quasi-equilibrium rate constant of adsorption, λ is distance between the two adjacent adsorption sites on solid surface, v_{tpcl} is the TPCL velocity, Ca is capillary number, capillary length is given as $L_{cap}=\sqrt{\frac{2\sigma_{lg}}{\rho_l g}}$ and L_s is

slip length where the usual no-slip boundary condition of classical continuum mechanics does not hold true.

For simplification purpose, the contact line velocity, v_{tpcl} in Eq. 10b was approximated by the impact velocity of the particle, v_{pA} at position A. The molecular parameters K_w, λ, and L_s are indeed fitting parameters which need to be obtained experimentally. The values used here were $K_w = 10^6\ s^{-1}$, $\lambda = 10^{-9}$ m, $L_s = 24.8 \times 10^{-9}$ m obtained for air, water, and glass particle system from the work of Liu et al.[6] which are applicable to the system studied in this work.

At the bottom interface, the energy requirement, $E_{c,bf}$ to overcome the capillary force can be obtained by replacing θ with the receding contact angle, θ_r in Eq. 9 similar to the derivation of energy requirement at top interface to yield

$$E_{c,tf} = 2r_p \int dF_c = 2r_p \int_0^{\pi/2} 2\pi r_p \sigma_{lg} \sin(\theta_r - 2\alpha) d\alpha = 4\pi r_p^2 \sigma_{lg} \cos\theta_r \tag{11}$$

Equation 10b can also be used to compute θ_r if the appropriate molecular parameters for the receding case are known experimentally. In absence of any such reported parameters on the present system, experimentally measured θ_r was used instead to compute the energy term from Eq. 11. It should be noted that measurement of θ_r was performed on a dry surface which would be different on prewetted surface (particle is wetted when it emerges from the bottom interface) in a stricter sense due to presence of a precursor thin liquid film. However, measured θ_r on dry particle surface (22°) was close to the approximately measured receding contact angle (~18°) exhibited on the particle surface during ligament breakup. These two measurements were close and considering some obvious uncertainty associated with the contact angle measurement, such small deviation is not expected to have any significant impact on the corresponding model predictions.

During penetration of the top interface, a gas cavity forms which leads to increase in gas-liquid interface area at the expense of impact kinetic energy of particle. It was previously noted by Ozawa and Mori[15] that inclusion of this cavity formation is essential in computing the surface tension effect which otherwise significantly undermines its contribution. Recognizing the complexities associated with the cavity formation process, in their work this effect was only accounted by an empirical multiplier in the expression of surface tension force. We here present a theoretical approach to compute this additional surface energy requirement in forming the gas cavity. Knowing the surface area of the gas cavity, associated surface energy can be calculated as

$$E_{cavity} = S_{cavity} \sigma_{lg} \tag{12}$$

Determination of the surface area in Eq. 12 requires knowledge of the interface shape. The cavity formation process during penetration is a complex transient event which leads to dynamic depression of the interface. In the steady-state case, an estimation of this interface depression is possible through numerical solution of the Young–Laplace equation which equates the Laplace pressure due to interface curvature to the hydrostatic pressure arising from interface depression. The differential form of this equation[13] can be written as

$$\frac{\frac{d^2y}{dx^2}}{\left[1+\left(\frac{dy}{dx}\right)^2\right]^{3/2}} + \frac{\frac{dy}{dx}}{x\left[1+\left(\frac{dy}{dx}\right)^2\right]^{1/2}} - y = 0 \tag{13a}$$

where nondimensional spatial co-ordinates are given as $y = H/L_{cap}$ and $x = r/L_{cap}$, and H is the interface depression height.

The solution of Eq. 13a defines the interface shape at steady state. A specific solution of Eq. 13a could indeed to shown to result in a catenary profile which upon rotation around an axis of symmetry yields a minimal energy surface called catenoid often used to define shape of interfaces like capillary bridge and soap film.[16] A complete catenoid geometry can be defined by a radius, $r_{cav,t}$ of two end rings of equal area, and a smaller ring at the center of radius $r_{cav,c}$ (please refer to Figure A1 in Appendix). On this basis, the shape of the catenary relating these two radii and height of interface depression, H can be described as follows

$$r_{cav,t} = r_{cav,c} \cosh\left(\frac{H}{2r_{cav,c}}\right) \tag{13b}$$

As at steady state, particle is attached at the central ring, it could be readily shown that $r_{cav,c}$ can be substituted by the radius of TPCL, $r_{tpcl,t}$. Computation of $r_{cav,t}$, therefore, requires determining parameter H, the only unknown variable which can be computed from the Young–Laplace equation (Eq. 13a). There are reported algebraic expressions[13] which are obtained by fitting the solution of Eq. 13a and can be used to determine an approximate yet accurate enough estimation of H instead of solving it directly by numerical integration. Based on the capillary length (L_{cap}) of the system in the range of $0.2 \le r_{tpcl,t}/L_{cap} \le 2.0$ where $r_{tpcl,t}$ represents the radius of the TPCL at top interface, for all penetration angle β, H can be approximated by the following expression[13]

$$H = L_{cap} a \sin(c\beta) \tag{13c}$$

where the fitting parameters a and c in Eq. 13c are given as

$$a = \frac{2.186}{1 + 0.649\left(\frac{L_{cap}}{r_{tpcl,t}}\right)} \tag{13d}$$

$$c = 0.5 + 0.332\left(-\frac{2.122 r_{tpcl,t}}{L_{cap}}\right). \tag{13e}$$

Angle β was derived corresponding to the maximum capillary force obtained by differentiating Eq. 9 with respect to β and equating it to zero. This leads to an interesting relation of $\alpha = \beta = \theta/2$ and $r_{cav,c} = r_{tpcl,t} = r_p \sin(\theta/2)$.

All parameters now being defined, the surface area of the catenoid can be given as[16]

$$S_{cavity} = \pi r_{cav,c}^2 \left[\cosh^{-1}\left(\frac{r_{cav,t}}{r_{cav,c}}\right) + \frac{1}{2}\sinh\left(2\cosh^{-1}\left(\frac{r_{cav,t}}{r_{cav,c}}\right)\right)\right] \tag{13f}$$

The surface area computed from Eq. 13f is half of the actual catenoid considering the shape has a mirror image around the center plane, that is, the TPCL. The complete derivation of Eq. 13f is provided in Appendix. The total contributions due to the surface tension force finally can be determined by summing up the energy expressions from Eqs. 10a, 11, and 12.

Particle-liquid film interaction outcomes

Intuitively, it could be readily realized that particle-film interactions would depend on the relative magnitude of the

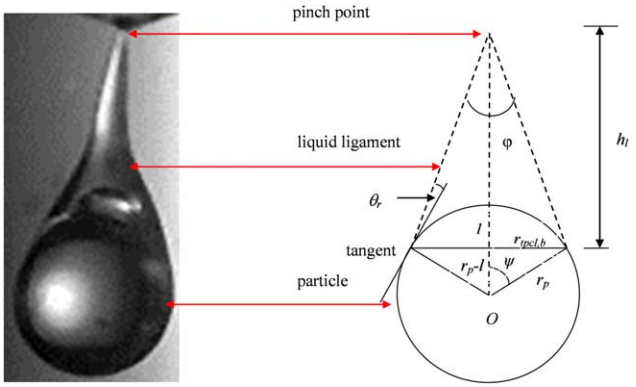

Figure 4. Experimentally observed liquid ligament shape attached to particle surface (left) and equivalent conical shape volume of the ligament used in the model (right).

[Color figure can be viewed in the online issue, which is available at wileyonlinelibrary.com.]

particle kinetic energy and the different work terms described earlier. Now, defining a collision parameter, C as the ratio of energy loss due to work terms described in Eqs. 7, 8, 10a, 11, and 12 to the available impact kinetic energy of the particle as

$$C=\frac{E_b+E_d+E_c}{\frac{1}{2}\left(\frac{\pi d_p^3\rho_p}{6}\right)v_{pA}^2} \tag{14}$$

and following further algebraic manipulations, C could be expressed as a function of dimensionless terms as

$$C=\frac{2S_{r1}}{\rho_r Fr^2}+\frac{1.5C_dS_{r1}}{\rho_r}+\frac{12(\cos\theta_a+\cos\theta_r+S_{r3})}{We\rho_r} \tag{15}$$

where $S_{r1}=l_f/d_p$ (ratio of film thickness to particle diameter), $S_{r3}=S_{cav}/\pi d_p^2$ (surface area ratio of gas cavity to particle), $\rho_r=\rho_r/\rho_f$ (density ratio of particle to film), Weber number $(We)=\rho_l v_p^2 d_p/\sigma$, Reynolds number $(Re)=\rho_l v_p d_p/\mu_l$, and Froude number $(Fr)=v_p/\sqrt{(gd_p)}$.

The magnitude of collision parameter, C determines the particle-liquid film collision outcomes. If $C>1$, the resistance to film penetration is relatively high and particle is captured/retained in the film. Conversely, when $C<1$, the impact inertia of particle overcomes all resistances in the film and results in complete penetration.

Liquid mass entrainment with particle

A collision parameter was defined in Eq. 15 which simply indicates that a collision interaction may result in a complete penetration outcome only when the available energy of the particle is higher than the energy spent to overcome the resistive forces in the film. In this section, a model is proposed based on the previously developed energy balance approach to quantify liquid mass entrainment with particle during the complete penetration outcome.

Referring to system energy balance in Eq. 6, all the work terms (W) being defined earlier in Eqs. 7, 8, 10a, 11, and 12, it could be realized that the equation contains two major unknowns—particle-ligament velocity V_{plB} and entrained liquid mass m_l. If interfacial area of film is assumed to remain unchanged before and after particle impact, that is, $S_{fA}=S_{fB}$, neglecting the some dissimilarity in the curved interface shape at top and bottom interface, Eq. 6 can be rewritten as

$$\left[\pi d_p^2\sigma_{lg}\cos\theta_s+\frac{1}{2}\left(\frac{\pi d_p^3\rho_p}{6}\right)v_{pA}^2+\left(\frac{\pi d_p^3\rho_p}{6}\right)gh_l\right]_A-\left[\frac{1}{2}\left(\frac{\pi d_p^3\rho_p}{6}+m_l\right)v_{plB}^2+\left(\frac{\pi d_p^3\rho_p}{6}+m_l\right)gh_2+S_{lig}\sigma\right]_B=-W \tag{16}$$

Solution of Eq. 16 also needs knowledge of ligament surface area S_l which requires a geometry to be defined. Figure 4 presents an experimentally obtained image of the liquid ligament connected to particle just before breakup (left). The shape of ligament could be defined approximately by a comical geometry which is shown in the schematic (right). Assigning an arbitrary angle ψ to denote the position of TPCL at bottom interface where the ligament adheres to the particle surface, the new surface area, S_l in form a cone of height, h_l and base radius equal to $r_{tpcl,b}$ can be calculated as

$$S_l=\pi r_{tpcl}\left(\sqrt{h_l^2+r_{tpcl,b}{}^2}\right) \tag{17}$$

Determining S_l requires computation of h_l which presumably is a function of residual particle inertia and $r_{tpcl,b}$. Knowing the particle-ligament velocity, v_{plB} and distance traveled at this speed within the time duration in which the ligament forms and breaks, the ligament height, h_l can be computed. A characteristic time scale[17] often applied to estimate the liquid jet/ligament breakup time, t_{lb} considering the effect of two major competing forces—inertia and surface tension is given as

$$t_{lb}\sim\sqrt{\frac{\rho_l r_{lig}^3}{\sigma}} \tag{18}$$

where r_{lig} is ligament radius.

However, unlike a typical uniform cylindrical jet which has a characteristic length scale represented by the nozzle radius, the closest length scale in particle-induced liquid ligament formation can be considered as the TPCL radius, $r_{tpcl,b}$ which again actually changes in time. Also, the driving force in formation of ligament, the particle inertia, decreases in time due to work done against the resistive effects in film which again is contrary to a typical cylindrical jet breakup case where nozzle velocity remains unaltered at the tip. In view of the above, $r_{tpcl,b}$ was used as a suitable length scale and a proportionality constant, K was introduced in Eq. 18 as a multiplier to account for any uncertainty in determining the ligament radius. Ligament breakup time t_{lb} was therefore obtained as

$$t_{lb}=K\sqrt{\frac{\rho_l r_{tpcl,b}^3}{\sigma}} \tag{19}$$

From geometric consideration in Figure 4, $r_{tpcl,b}=r_p\sin\psi$ where the polar angle, ψ can be obtained as $\psi=0.5(\pi-\varphi)-\theta_r$ if both cone angle, φ and receding contact angle θ_r are known *a priori*. In case of breakup of axisymmetric near inviscid fluid ligament at dripping state, it has previously been shown numerically that cone angle, φ during pinch-off acquires a unique value of 18.1°.[18] This finding was later corroborated by Castrejon-Pita et al.[19] experimentally using high speed imaging of the dripping behavior of water and ethanol droplets where this cone angle found to vary consistently within 17.9 ± 0.2°. Noting the similarity between the droplet dripping

process and the particle-induced ligament breakup studied here, a value of $\varphi = 18°$ was used in Eq. 19. The receding angle, θ_r was experimentally measured and a value of 22° was used for computation purpose (see Table 1). With all parameters being known, ligament height, h_l from Eq. 19 was determined as

$$h_l = v_{plB} t_{lb} \tag{20}$$

The geometry of the conical-shaped ligament surface area, S_l now being defined; entrained liquid mass m_l could be calculated if it is assumed that no secondary droplet is formed after breakup which may or may not attach to particle. With this assumption, m_l was determined from the geometry of conical ligament shown in Figure 4 as

$$m_l = \left[\frac{\pi r_{tpcl,b}^2 h_l}{3} - \frac{\pi d_p^3}{24}\left(2 - 3\cos\psi + \cos^3\psi\right)\right]\rho_l \tag{21}$$

where the first and second term of the right-hand side of Eq. 21 represents the cone volume and spherical cap volume of particle inside the ligament, respectively.

It would now appear that both parameters S_l in Eq. 17 and m_l in Eq. 21 require only one unknown variable, that is, particle-ligament velocity, v_{plB} to compute the entrained liquid mass, m_l if the proportionality constant K in Eq. 19 is known beforehand. Also, the work term due to fluid drag (Eq. 8) requires an average velocity at positions A and B defined as $(v_{pA} + v_{plB})/2$ which involves the unknown parameter v_{plB}. Both v_{plB} and K were obtained iteratively by solving Eq. 16 using a Newton–Raphson algorithm suitable for solution of nonlinear algebraic equations. In the solution procedure, at first guess values for both the parameters were used. For a fixed value of K, v_{plB} was solved iteratively satisfying the energy balance in Eq. 16 by setting the residual error value to a convergence limit of 10^{-6}. Proportionality constant K was used as a fitting parameter which was obtained after several iterations by minimizing the sum of square errors between the experimental measurements and the model predictions of m_l.

CFD Modeling

To simulate the interactions phenomena, a two-phase 3-D incompressible CFD model using interface capturing VOF approach was utilized in the finite volume method-based commercial CFD solver ANSYS Fluent (ver. 14.5) coupled with dynamic meshing algorithm to simulate the particle motion.[3] The computational geometry and boundary conditions used in the CFD model are presented in Figure 5. The developed CFD model in Cartesian coordinates comprising continuity, momentum, and volume fraction equations was solved as follows[20]

$$\frac{\partial \rho_{mix}}{\partial t} + \nabla.(\rho_{mix}\vec{v}) = 0 \tag{22}$$

$$\frac{\partial(\rho_{mix}\vec{v})}{\partial t} + \nabla.(\rho_{mix}\vec{v}\vec{v}) = -\nabla P + \nabla.\left[\mu_{mix}(\nabla\vec{v} + \nabla\vec{v})^T\right] + \rho_{mix}\vec{g} + \vec{F}_s \tag{23}$$

The VOF method includes a single momentum equation for both phases and uses volume fraction averaged transport properties. The mixture density, ρ_{mix}, and viscosity, μ_{mix}, were calculated based on the individual phase volume fractions, α as

$$\rho_{mix} = \alpha_l \rho_l + \rho_g(1 - \alpha_l) \tag{24}$$

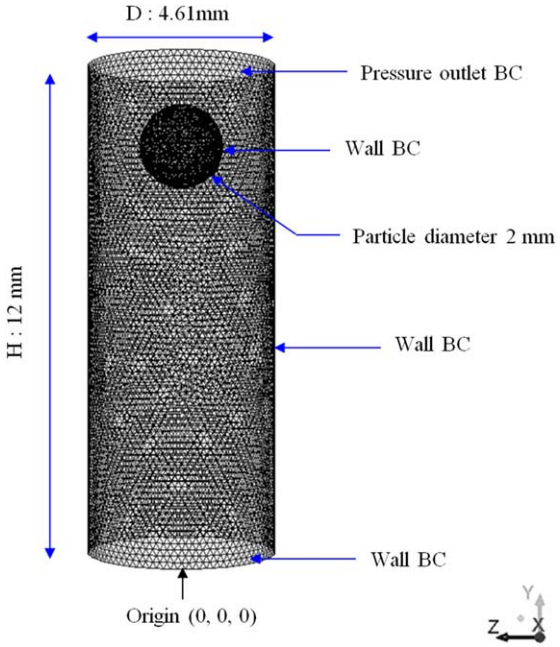

Figure 5. Computational domain showing the geometry, mesh, and boundary conditions used in the 3-D CFD model.

[Color figure can be viewed in the online issue, which is available at wileyonlinelibrary.com.]

$$\mu_{mix} = \alpha_l \mu_l + \mu_g(1 - \alpha_l) \tag{25}$$

where ρ and μ refer to phase density and viscosity and subscript l and g refer to liquid and gas phase, respectively.

The volume fraction of the dispersed phase (which is liquid here) used in Eqs. 24 and 25 was determined by solving the following advection equation

$$\frac{\partial \alpha_l \rho_l}{\partial t} + \vec{v}.\nabla(\alpha_l \rho_l) = 0 \tag{26}$$

while the phase fraction of the continuous phase (gas) was calculated using the following conservation equation

$$\sum_{i=1}^{2} \alpha_i = 1.0 \tag{27}$$

The momentum equation, in addition to pressure, gravity, and viscous stress, included a density averaged surface force term, F_s where

$$F_s = \frac{\sigma_{lg}\rho_{mix}\kappa\nabla\alpha_l}{0.5(\rho_l + \rho_g)} \tag{28}$$

It can be noted that surface tension force is a line force, in principle, however, in the present CFD solver framework a body force (volumetric) form of this source term was used to keep parity with the unit of other terms in Eq. 23.

The local curvature of gas-liquid interface κ used in Eq. 28 was computed as divergence of the unit normal vector obtained from the surface normal vector on the interface as follows

$$\kappa = \frac{1}{|n|}\left[\left(\frac{n}{|n|}.\nabla\right)|n| - (\nabla.n)\right] \tag{29}$$

The surface normal vector, n in the VOF approach can be written as gradient of phase volume fraction at the interface

noting the fact that gradient vector of a surface is orthogonal to the tangent at any point on the surface. On liquid side of the interface, this was written as

$$n = \nabla \alpha_l. \tag{30}$$

A solid surface can exhibit either wetting or nonwetting behavior depending on the solid surface energy. When surface energy is high, the adhesion force between solid and liquid is quite significant which leads to complete wetting of the surface. On the contrary, less surface energy results into lower adhesion force which leads to partial wetting or complete dewetting of the surface. This adhesion characteristic at wall was modeled using a contact angle boundary condition. At wall, two unit vectors were considered which are oriented to normal and tangential direction, respectively. The unit vector in normal direction, $\hat{n}_w$ points to fluid while the unit vector in tangential direction, $\hat{t}_w$ indicates wall. Unit normal $\hat{n}$ was expressed as a function of contact angle, θ (defined as the angle between the tangent vector at wall and tangent vector at the interface—see Figure 3b) as follows

$$n = \hat{n}_w \cos\theta + \hat{t}_w \sin\theta \tag{31}$$

In a dynamic scenario where TPCL forms on the solid surface, modeling of contact angle boundary condition is known to be a complex problem due to the fact that contact angle changes dynamically with the contact line velocity. A rigorous mathematical treatment of the moving contact angle problem was reported by Shikhmurzaev[21] based on his earlier work[22] which specifically focused on obtaining a generalized expression of the dynamic contact angle as a function of contact line velocity. Three flow regions were considered—first, a narrow inner region near the contact line ($Ca \ll 1$) where the viscous stresses are comparable to surface tension gradients, second, an intermediate region having dimension of apparent slip length where surface tension gradient occurs and finally an outer region comprising bulk fluid where the surface tension gradient disappears. In his analysis, the unbound shear stress problem at the contact line was resolved using an appropriate slip boundary condition. The contact line motion was attributed to the surface tension gradient between the contact line region and the bulk liquid which was explained by a surface equation of state. The macroscopic dynamic contact angle was related to the contact line velocity and few other empirical surface parameters. Implementation of this complex model in the present CFD modeling framework was beyond the scope of this study, however, a set of simulations were performed using the experimentally measured values of constant advancing, static, and receding contact angle to demonstrate the sensitivity of this critical boundary condition on correct representation of overall physics of the problem.

A 3-D cylindrical geometry [ID: 4.61 mm $\times$ 12 mm (H)] with unstructured grid containing 320,256 tetrahedral cells was used in the simulation. For modeling wall adhesion, the contact angles values reported in Table 1 for water on glass particle surface and on capillary tube surface were applied. On both particle and capillary tube wall, a no-slip boundary condition was specified. Pressure outlet boundary condition (zero gauge pressure) was used at the top face of the capillary tube while a wall boundary condition (BC) was used at tube bottom.

A second-order upwind scheme was used for discretization of the momentum equation while the volume fraction parameter and pressure were discretized using Geo-Reconstruct and Presto scheme, respectively. Pressure-velocity coupling was obtained by PISO scheme. A residual of 10^{-4} was set for convergence of continuity, momentum, and volume fraction equations. To initialize the simulation, a liquid film was introduced by patching liquid volume fraction equal to one. The thickness of the liquid film used in the simulation was the average film thickness obtained from experimental measurement mentioned before. All simulations were performed using a time step size of 10^{-6} s with 50–100 iterations ensuring convergence per time step.

To model the solid particle motion, a dynamic meshing technique was used involving smoothing and remeshing scheme on the adjacent cells of particle boundary. The smoothing scheme involved stretching of cells adjacent to the moving surface using a spring constant based on Hooke's law. A spring constant of 0.5 was used in the present model. When cell motion is large, cells around the moving wall deform heavily and become highly skewed. To avoid simulation failure, these cells requires remeshing. For computational efficiency, only the cells which exceeded a specified skewness of 0.7 and a predefined range of cell size (min. to max.) were remeshed. The particle was considered to be a rigid body and its motion was obtained by implementing a user defined function based on a six degree of freedom solver embedded in Fluent. Due to low impact Weber number and very insignificant visible rotation in the experiment, the rotational motion of the particle was not simulated in the present work.

Results and Discussions

Particle-film collision outcomes

In the experiment, interaction between particle and the film was studied in the particle Weber number range of 1.3–33. Depending on the impact Weber number, three distinct interaction types were observed—particle retention at top interface, particle penetration through top interface but retention at bottom interface, and complete penetration through both interfaces. Experimental observations and CFD model predictions at different time instances are presented in Figures 6a–c.

Figure 6a presents a low Weber number case ($We = 1.4$) of particle-film interaction. Here, as the particle slowly descends, the TPCL rises over the particle surface and when particle kinetic energy is completely dissipated to overcome the resistive forces (capillary, buoyancy, and viscous force) in the film, particle gradually comes to a steady partial submergence state with decaying amplitude of oscillation at the interface. The iso-surface contours of the interface colored by the volume fraction of liquid-film) obtained from by the CFD model are also presented at the same time instances. Among all the contact angles BCs used, the static contact angle BC was found to be most suitable to simulate this low Weber number case (CFD model predictions with advancing and receding contact BC not shown here). This can be explained by the gradually decaying motion of the particle at interface which leads to nearly zero TPCL motion ($Ca \sim 0$) and consequently the dynamic contact angle settles around a static contact angle value. This can also be shown using Eq. 10b which yields a static contact angle when the contact line velocity containing terms in the expression are set to zero. The model predicted partial submergence behavior of the particle at the top interface compares well with the experimental observation (see the Supporting Information video file titled *capture case top interface* online).

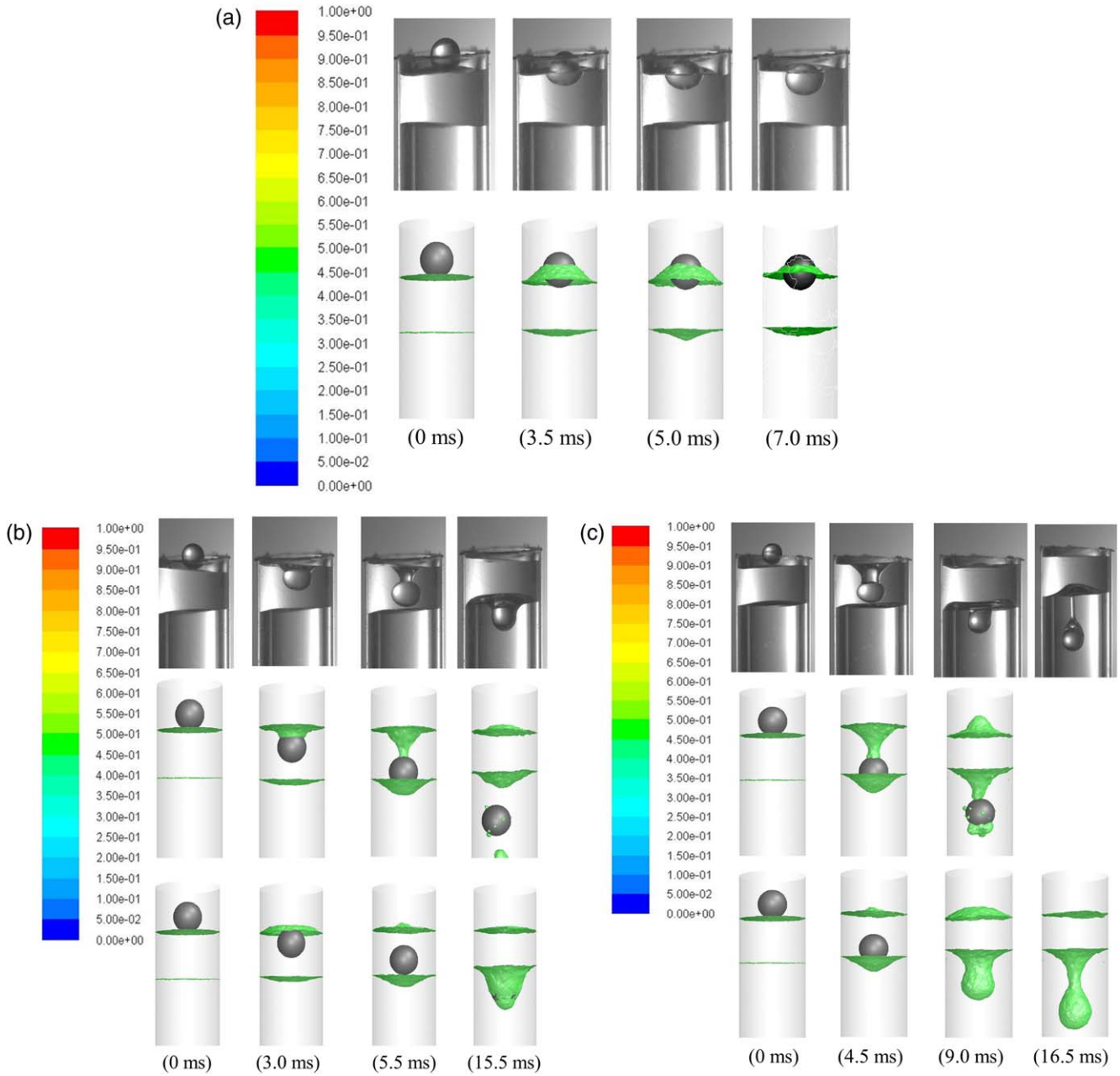

Figure 6. Comparison of experimental observations and CFD modeling predictions of particle-liquid film interactions behavior ($d_p = 2.05$ mm) at (a) *We*-1.4: particle retention at top interface; - experiment (top row) CFD model with static contact angle BC, $\theta_s = 51^\circ$ captures the partial submergence behavior of particle behavior well (bottom row), (b) *We*-11.7: particle retention at bottom interface—experiment (top row); CFD model with advancing contact angle BC, $\theta_a = 110^\circ$ captures the gas cavity formation at top interface reasonably well but predicts early nonphysical detachment at bottom interface (middle row); CFD model with receding contact angle BC, $\theta_r = 22^\circ$ does not predict the gas-cavity formation at top interface but reasonably predicts deformation behavior at bottom interface (bottom row), and (c) *We* = 22.5: complete penetration of both interfaces—experiment (top row); CFD model with advancing contact angle BC, $\theta_a = 110^\circ$ predicts interaction dynamics well at top interface (middle row); and CFD model with receding contact angle BC, $\theta_r = 22^\circ$ provides good agreement at bottom interface (bottom row).

[Color figure can be viewed in the online issue, which is available at wileyonlinelibrary.com.]

At an intermediate Weber number ($We = 11.7$), the particle penetrates through the top interface while attaining a partial penetration through the bottom interface (Figure 6b). A gas cavity can be seen forming at the top interface ($t = 4.5$ ms) which eventually snaps off as the radius of TPCL gradually diminishes to zero with increasing penetration depth. Being located just above the bottom interface at $t = 4.5$ ms, it requires almost same time (4.5 ms) for the particle just to penetrate through the bottom interface ($t = 9.0$ ms) due to significant loss of kinetic energy against the opposing forces inside the film. CFD model with the contact angle BC of $\theta_{adv} = 110^\circ$ predicts formation of this gas cavity which evidently is in

good agreement with the experiment. TPCL velocity here is significant ($0 < Ca < 1$) due to higher impact velocity of particle which leads to occurrence of a larger dynamic advancing contact angle on particle surface. Also, important here to notice the swelling of the top interface ($t = 9.0$ ms) which is caused by an upward motion of the liquid in the film center leading to formation of a mild jet just after occurrence of the cavity snap-off event. Such swelling at top interface was also visualized in the experiment. The other simulations using static and receding contact angle BCs (not shown) do not predict this gas cavity formation process and emphasizes the fact that adequate treatment of the contact angle is indeed required to capture the correct flow dynamics. At the bottom film interface, further motion of the particle is prohibited by the capillary force ($t = 15.5$ ms) which pulls back the particle in the upward direction causing a rebound at the bottom interface. The particle then gradually settles down at the bottom interface after few oscillations with decaying amplitude (see the Supporting Information video file titled *capture case bottom interface* online). At this later stage of particle-film interactions, it could, however, be noticed that once the gas-cavity snaps off, the advancing contact angle boundary condition of the CFD model no longer suffices which incorrectly manifests itself in an early detachment process of particle from the liquid ligament at t ~11 ms as opposed to experimental observation which indicates particle is attached to bottom interface even at $t = 15.5$ ms. This anomaly, however, is resolved when a receding contact angle BC is used which presents the dynamics at the bottom interface in a better physically plausible manner.

At higher Weber number cases (e.g., $We = 22.5$), the particle has sufficient kinetic energy to overcome all the resistive forces and penetrates through the film completely (Figure 6c). During penetration of the top interface when gas cavity collapses, a bubble was observed to attach to the particle surface consistently ($t = 16.5$ ms). This bubble entrainment phenomenon was also noted by Dubrovsky et al.[12] in context of droplet-particle collision process at higher impact velocities. The bubble entrapment phenomenon is known to occur due to certain instability arising out of deformation of interface at the TPCL area.[22,23] In the complete penetration case, a liquid ligament forms which keeps the particle attached to the bottom interface. The ligament finally breaks off leading to some liquid mass entrainment with the particle forming at least one trailing secondary droplet (see the Supporting Information video file titled *complete penetration case* online). The CFD model presents two limiting cases using advancing ($\theta_a = 110°$) and receding ($\theta_r = 22°$) contact angle BC. Similar to $We = 11.7$ case, the dynamics at top interface involving the gas-cavity (interface depression) is captured well with the use of advancing contact angle BC. At the bottom interface, although the formation of the ligament is better represented with receding contact angle compared to advancing contact angle BC, the final ligament breakup could not be captured which occurred sometime later (>19.5 ms, not shown). This can be again attributed to the inadequate resolution of the ligament interface because of unstructured dynamic mesh which undergoes significant deformation during simulation. It should be noted that due to early detachment ($t \sim 11.0$ ms) of the particle from the connecting ligament in the advancing contact angle BC scenario, no simulation snapshot is available for time instance at $t = 16.5$ ms for comparison.

The contact angle BC sensitivity analysis shows that a single contact angle BC does not suffice to present the complete dynamics of particle-film interactions and indeed requires implementation of a rigorous dynamic contact angle BC in the CFD model. The perceivable problem with the implementation of molecular-hydrodynamic type contact angle models (Eq. 10b) reported in the literature is with the fitting parameters such as molecular slip length and liquid adsorption rate constant which need to be obtained experimentally for a specific system.[6,14] Given the dimension of molecular slip length scale which is in the order of few nanometers, understandably it would be computationally very expensive to resolve the slip region close to TPCL.[23]

On the other aspect, we noted that few previous studies focused on implementing dynamic contact angle model in CFD code to simulate phenomena like drop spreading and recoiling on solid surface.[23,24] These studies used dynamic contact angle model based on contact line velocity and determined the advancing and receding contact angle BC based on the sign change in the contact line velocity using axisymmetric geometry. It is worthwhile to mention that Sikalo et al.[23] reported good agreement of their CFD model predictions with the experimental measurements without specifically addressing the molecular nature of the contact angle. They reasoned this to the inertial nature of the contact line motion ($Ca > 0$) which is possible to capture solely by an appropriate macroscopic dynamic contact angle boundary condition. The presently investigated scenario is arguably has more complexities where no velocity reversal (sign change) occurs in the complete penetration case making it even more difficult to implement any previously reported dynamic contact angle modeling methodology and requires further research by its own merit.

Particle motion inside film

It is of interest to look into the particle motion profile during these interactions which brings the perspective of different resistive forces responsible for inhibition of particle motion. Figures 7a–c compares the experimentally obtained particle velocity profiles with the CFD model predictions with different contact angle BCs obtained in the low to high Weber number cases corresponding to the visuals presented in Figures 6a–c.

Figure 7a presents the dynamics at $We = 1.4$ until 7 ms only where the particle has not come to a completely stationary state yet. The velocity gradually decreases as kinetic energy is spent to overcome counteraction of the resistive forces. It can be seen that CFD model predictions using advancing contact angle BC indicate a reasonable agreement with experimental measurements in the early stage of interactions, however, it does not show the trend of particle gradually coming to a motionless state in later stages which is actually better predicted by the static contact angle BC. This could be explained by presence of nonzero TPCL velocity in the early stage of interactions which results in a contact angle value higher than static contact angle, however, toward the end of the interaction, the state of nearly zero TPCL velocity leads to a static contact angle value on particle surface. Receding contact angle BC, on the other hand, predicts an early zero motion state due to higher wetting characteristic which leads to faster submergence followed by a slightly upward movement.

In Figure 7b, dynamics at intermediate Weber number ($We = 11.7$) was presented where the particle can be seen rebounding from bottom interface after impact at ~18 ms due to opposing capillary force. Both static and receding contact angle BC scenarios indicate this rebound behavior but predict

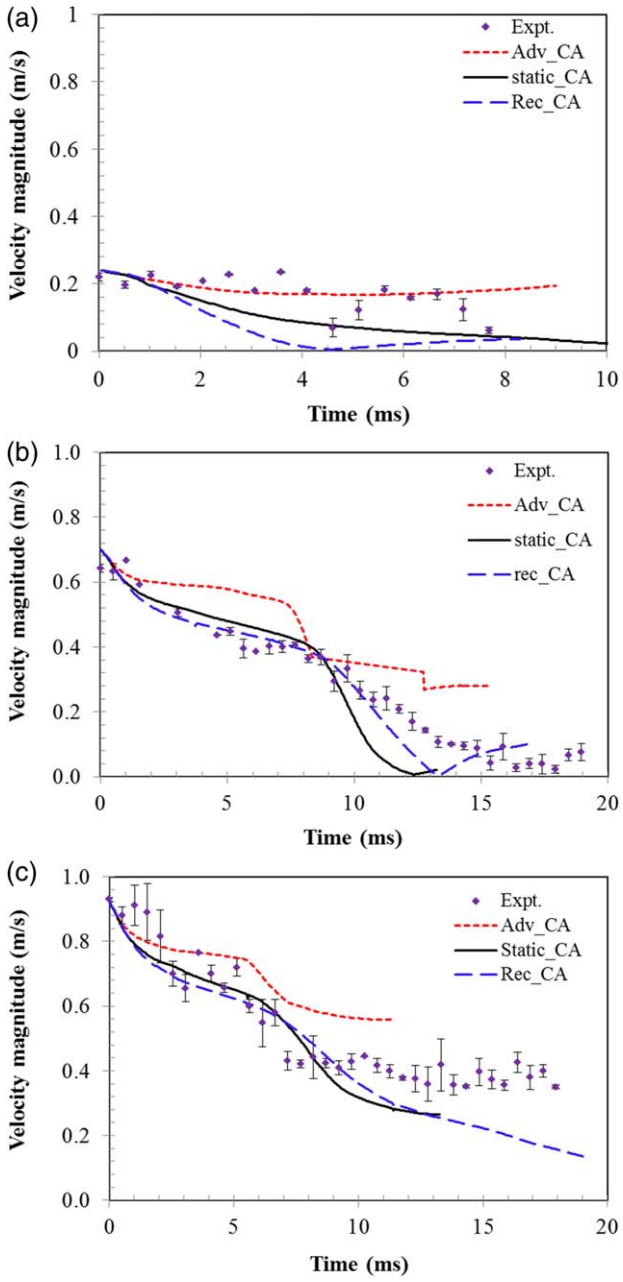

Figure 7. Comparison of experimentally found particle velocity profile and CFD model predictions during particle-liquid film interactions (d_p = 2.05 mm) at (a) *We* = 1.4, (b) *We* = 11.7, and (c) *We* = 22.5.

[Color figure can be viewed in the online issue, which is available at wileyonlinelibrary.com.]

the reversal of particle velocity somewhat earlier at ~12 and 13 ms, respectively. The advancing contact angle BC, however, could not represent this dynamics and rather indicates a nonphysical outcome of early detachment of particle from ligament ($t \sim 11$ ms). This is again due to inability to represent the true fact that at bottom interface a more receding type contact angle is exhibited during stretching of the bottom meniscus, which significantly alters magnitude of the opposing capillary force. Conversely, early prediction of the rebound by the other two BCs can be attributed to inability to capture the gas cavity formation at top interface which affects the penetration process.

Figure 7c presents the particle motion profile in the higher Weber number case ($We = 22.5$). Particle here penetrates the bottom interface at ~9 ms and then pulls down the bottom meniscus to form a conical-shaped ligament which breaks up at ~17 ms (Figure 6c). Interestingly in this duration, the particle velocity remains almost constant as the ligament keeps expanding at a constant velocity till the breakup occurs. Considering contribution of inertia and surface tension force alone, a velocity scale for the ligament can be established as $v_{lig} \sim \sqrt{\frac{\sigma}{\rho_{lig} r_{lig}}}$. Effect of viscosity in this formulation can be ignored given the low range of Ohnesorge numbers ($Oh = \sqrt{We}/Re$): 0.0022–0.0034 used in the present study. This scaling indeed yields a lower velocity, for instance in *We*-22.5 case, it gives a velocity of ~0.26 m/s which is less than the experimentally obtained particle-ligament system velocity ~0.4 m/s. The deviation can be reasoned to few different factors such as uncertainties in particle inertia due to particle shape irregularities, difficulty in defining the ligament radius due to its conical shape and slip between particle velocity and TPCL velocity which remains unaccounted in the present analysis.

The CFD model predictions of particle velocity within the film specifically using static and receding contact angle BC agree well with the experimental measurements up to $t \sim 9$ ms. Some deviations in the CFD model predictions afterward are quite apparent for all contact angle boundary conditions. In contrast to experiments, these deviations include early detachment of particle from ligament ($t \sim 11$ ms) for advancing contact angle BC, continual decreasing velocity profile for receding contact angle BC and lastly a relatively flatter velocity profile for static contact angle BC scenario. Furthermore, the conical shape of the ligament as observed in the experiment was not predicted by the CFD model, which can be attributed to inadequate resolution of the interface due to use of unstructured mesh. Admittedly, the use of unstructured mesh is a big impediment for VOF simulation which ideally requires fine structured mesh for accurate construction of interface. This was indeed a limitation in the present CFD model due to inclusion of dynamic meshing technique for particle motion which essentially requires unstructured mesh for large rigid body motion.[3] Alternative approach to simulate such complex physics could be use of coupled VOF method for treatment of free surface flow and Immersed Boundary (IB) method for simulating particle motion to prevent mesh deformation. Although studies in this area involving use of such coupled numerical approach are actually very limited, one such work by Deen et al.[25] demonstrates simulation of a single particle sinking through a single flat liquid interface. The simulation shows formation and breakup of gas cavity as the particle descends through interface similar to results obtained in this study, however, the gas cavity shape was much narrow compared to our experimental visualizations which possibly could be attributed to the different physical properties of the liquid used in their work (100 times higher viscosity and 1.38 times higher surface tension value compared to this study). It is not although clear how the adhesion behavior at the particle surface was treated as there was no mention of contact angle in their model. Also, no experimental validation of this simulation was presented which could substantiate the model predictions.

Table 2. Comparison of Particle-Film Interaction Predicted by Collision Parameter (C) and the Experimental Outcomes

Particle Diameter (d_p) (m)	Impact Velocity (v_p) (m/s)	Weber Number (We)	Collision Parameter (C)	Interaction Outcome (Exp.)
0.00215	0.217	1.38	9.75	Retention
0.00199	0.500	6.84	2.12	Retention
0.00201	0.651	11.65	1.45	Retention
0.00201	0.780	16.75	1.16	Penetration
0.00199	0.907	22.49	1.00	Penetration
0.00183	0.281	1.98	6.87	Retention
0.00164	0.452	4.60	3.32	Retention
0.00187	0.658	11.11	1.64	Retention
0.00180	0.931	21.38	1.12	Penetration
0.00174	0.951	21.59	1.13	Retention
0.00152	0.263	1.44	10.29	Retention
0.00155	0.561	6.71	2.60	Retention
0.00149	0.650	8.63	2.22	Retention
0.00159	0.838	15.29	1.54	Retention
0.00167	1.024	23.95	1.22	Penetration
0.00136	0.268	1.34	11.69	Retention
0.00135	0.583	6.30	2.94	Retention
0.00129	0.638	7.17	2.78	Retention
0.00141	0.844	13.78	1.75	Retention
0.00146	1.013	20.55	1.40	Penetration
0.00122	0.324	1.76	9.62	Retention
0.00134	0.422	3.27	5.28	Retention
0.00124	0.757	9.77	2.39	Retention
0.00125	0.985	16.58	1.79	Retention
0.00122	0.964	15.61	1.80	Retention
0.00237	0.915	27.23	0.76	Penetration
0.00247	0.914	28.25	0.72	Penetration
0.00223	0.917	25.65	0.82	Penetration
0.00208	0.918	24.05	0.88	Penetration
0.00183	0.921	21.24	1.04	Penetration
0.00291	0.909	32.94	0.60	Penetration
0.00257	0.913	29.32	0.69	Penetration
0.00280	0.910	31.79	0.62	Penetration
0.00270	0.912	30.71	0.65	Penetration

Regime boundary demarcation by collision parameter (C)

The collision parameter, C defined by Eq. 15 was used to obtain a regime boundary for the observed particle-film interactions. Table 2 lists the experimental observations of interactions outcome for different particle diameters and impact velocities. In all the cases, velocity containing terms in Eq. 15 were computed based on the particle velocity at position (A) to determine value of C. The collision parameter, C determines the collision outcomes by indicating $C > 1$ for the capture/retention case and $C < 1$ for the complete penetration case which agreed well with most of the experimental observations listed in Table 2. There were few exceptions to this criterion where particles were found to undergo a complete penetration at C values slightly greater than 1.0. The anomaly can be explained by some irregularity in shape of particles and particle orientation during impact which may affect all the force magnitudes which are computed based on the assumption of a perfect spherical body. Additionally, the various approximations used in the model such as constant magnitude of advancing/receding contact angle and interface inclination angle, quantification of surface energy for gas-cavity formation under a steady-state assumption and value of drag coefficient for the submerged particle essentially lead to some uncertainties in the computed force magnitudes. Generally speaking, this criterion in principle holds good elsewhere where the particle kinetic energy is too low or too high compared to overall film resistance. However, when these two competing parameters are comparable in magnitudes, that is, their ratio is close to 1.0 near the regime transition, any uncertainty in the force computation here would lead to a different outcome. This is evident from Table 2 where values less than 1.0 to slightly higher than 1.0 (maximum is 1.4) led to the outcome of particle penetration but values over it consistently predicted particle retention.

Figure 8 presents the trend of collision parameter, C computed from Eq. 15 against Weber number for minimum particle size (red solid line) and maximum particle size (black dashed line) used in experiment represented by parameter, S_{r2}. C values calculated based on the operating conditions used in experiments were also plotted (green filled squares). All the experimental points can be seen falling between the predictions for maximum and minimum values of the S_{r2} given as ratio of film diameter to particle diameter (df/dp) parameter. A good power law dependency of collision parameter C on Weber number ($R^2 = 0.9657$) fitted through the experimental points was obtained. The trend indicates parameter C inversely varies with the particle Weber number exponent value of $\sim$0.82. The correlation actually further simplifies the expression of C from Eq. 15 being dependent on just a single parameter, that is, particle Weber number. A theoretical prediction of critical Weber number for film penetration was obtained by intersecting an iso-C line ($C = 1.0$) with the model predicted trend lines for minimum and maximum value of S_{r2} parameter. The intersection yields a critical Weber number range between 5.8 and 270 for minimum and maximum S_{r2}, respectively. It can be noted that this critical Weber number for film penetration increases as S_{r2} parameter decreases, that is, particle diameter is reduced which also supports the intuitive logic that smaller particle would require higher impact velocity for penetrating the film of same thickness. In experiment, minimum Weber number for penetration was 16.75 (Table 2) which falls within this theoretically predicted range.

Ligament breakup

One of the interesting aspects of particle-film collision is liquid mass entrainment with particle during complete penetration. The phenomenon is of particular interest to quantify distribution of atomized liquid droplets among the solid particles

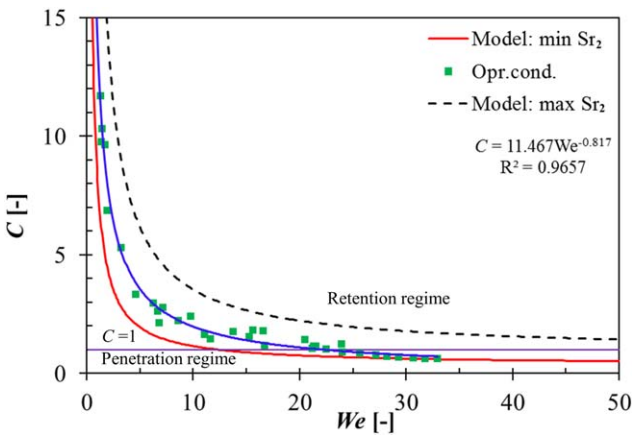

Figure 8. Collision parameter C predicted by the model for minimum and maximum S_{r2} parameter.

[Color figure can be viewed in the online issue, which is available at wileyonlinelibrary.com.]

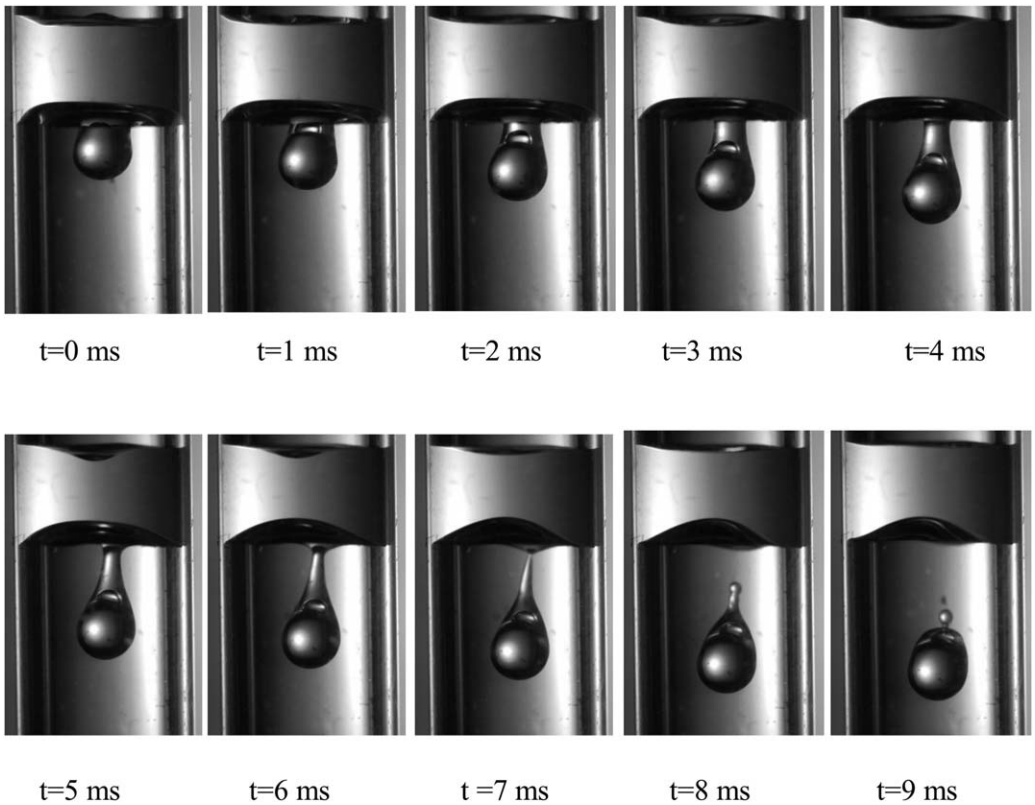

Figure 9. Formation and detachment of liquid ligament from the bottom film interface behind the moving particle by end pinching mechanism at different time interval ($d_p = 2.05$, $We = 22.5$).

Capillary waves visible only after the ligament pinches off from the bottom interface leading to formation of at least one secondary droplet.

in a gas-solid fluidized bed often involving collision-induced heat and mass-transfer process.[26]

Figure 9 presents a time sequence of high speed visualizations indicating formation of a liquid ligament-induced by particle inertia at the bottom film interface. During penetration of the bottom interface, a TPCL forms around the particle surface. As the particle further descends, TPCL moves in opposite direction resulting in formation of a conical-shaped liquid ligament connected to the falling particle. Due to the adhesion force between particle surface and liquid, the TPCL eventually stops moving further upward and a necking point is formed on the ligament close to bottom interface. The ligament can be seen gradually elongating and narrowing down in the radial direction at the necking position ($t = 4$–7 ms) due to the continuous downward motion of the particle. The ligament breaks up at $t = 7$ ms and following this, it can be noticed that ligament rapidly relaxes ($t = 8$ ms) due to surface tension force forming a small secondary droplet trailing behind ($t = 9$ ms). A bubble entrapment can also be noticed in the liquid cone resulting from snapping of the gas cavity at top interface.

The ligament breakup process in context of droplet-particle collision bears similarity with the cylindrical liquid jet breakup which results from the competitive interplay between flow instabilities due to shear (Kelvin–Helmholtz instability) or surface tension (Rayleigh instability) and stabilizing effect from viscosity.[27] Investigation of these critical parameters governing droplet generation resulting from liquid jet breakup is a mature field of two phase fluid dynamics research and several excellent studies are available.[17,27–29] On contrary, few studies are actually available on particle-induced ligament breakup during droplet-particle collision. Dubrovsky et al.[12] reported formation of liquid ligament during complete penetration type interaction between droplet and particle which further break into multiple smaller secondary droplets. The liquid carryover with particle was quantified empirically in terms of dimensionless numbers in their study, however, no physical mechanism for ligament breakup was proposed.

Hoeve et al.[17] identified three major mechanisms of droplet formation from liquid jet breakup namely dripping, jetting, and wind-induced on a regime map using orifice radius and jet velocity as coordinates. The dripping mechanism occurs at low flow rate ($We_{lig} < 4$) while jetting mechanism is dominant at higher flow rate ($We_{lig} > 4$) where We_{lig} is the Weber number based on ligament radius. The jetting mechanism for breakup also known as Rayleigh breakup, involves presence of capillary waves on ligament interface which are enhanced by the external mechanical or thermal disturbances. Some of the disturbances are favored by surface tension force which grows in magnitude comparable to the ligament circumference finally resulting into end pinch-off of the ligament to produce droplets. The third mechanism—wind-induced droplet generation involves external shearing action from a co/cross flowing gas stream on the ligament interface which disintegrates the jet to create droplets. As in the present study ligament breakup occurred in a quiescent environment, this mechanism for obvious reason was deemed to be not valid and therefore excluded from the further discussions on seeking a suitable mechanism for the particle induced ligament breakup.

In the higher Weber number case (We-22.5) using a ligament velocity ~0.4 m/s (Figure 7c) and considering particle radius r_p as the ligament length scale, a We_{lig} of 2.3 was obtained which confirms that ligament breakup occurred

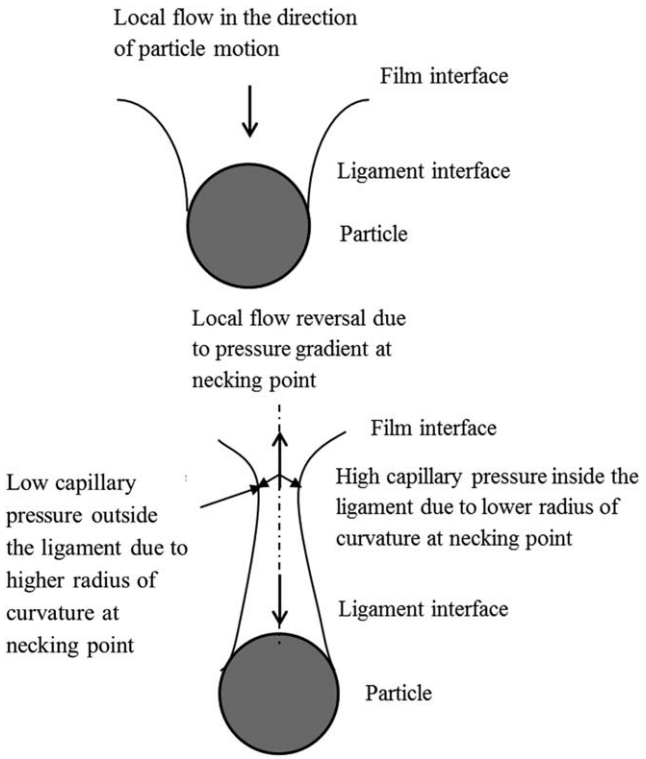

Figure 10. Schematic of (a) formation of ligament and (b) breakup of ligament by end-pinching mechanism during complete penetration of liquid film.

within the limit of dripping mechanism as previously suggested by Hoeve et al.[17] This is further substantiated by the fact that no capillary wave was observed on the ligament interface during breakup (Figures 4 and 9). In a related work of Dubrovsky et al.,[12] complete droplet penetration behavior by particle (droplet-particle size ratio > 1) was studied at relatively higher impact velocity characterized by the Reynolds number range from 9.51 to 6681 and Weber number range from 252 to 13,012 based on the impacting droplet diameter and relative velocity between droplet-particle pair. It would be noteworthy to mention that of the few interaction images of complete penetration scenario available from their work; also any presence of capillary wave on the ligament interface was not observed even at such high impact Weber number.

Absence of capillary wave in ligament breakup process during elongation of viscous droplet in four-roll mill under varying shear rate was also noted by Stone et al.[27] In their experiments, droplet was elongated into a ligament of certain aspect ratio under the applied shear rate. After a specific ratio was reached, shearing was discontinued and droplet was allowed to relax. Depending on the viscosity ratio and degree of elongation, either ligament breakup occurred or droplet returned to its initial spherical shape. When ligament breakup occurred, it was found that the ligament was independently produced only through pinching of the ligament ends connected to bulbous parts of the droplet. Even when elongation ratio was large enough so that length of the ligament was several times larger than its circumference, a critical requirement to be met for capillary wave growth to occur, no capillary instability was observed on the ligament interface. It was reasoned that "end-pinching" mechanism occurs at a time scale which is much shorter than the time required by very small capillary perturbation to grow up to finite amplitude. However, once the ligament breakup is initiated by the "end-pinching" mechanism, which ensures that a significant perturbation now exists in the ligament, surface tension can amplify it resulting into appearance of capillary wave instability in the remaining ligament before finally breaking it down into number of smaller secondary droplets.

In this study, small capillary waves were also observed on the cylindrical strand of the ligament part just after breakup (Figures 4 and 9) which led to formation of at least one secondary droplet. On the basis of present experimental observations and previously reported analysis, it can be therefore concluded that capillary instability is unlikely to cause the particle-induced ligament breakup and "dripping" or "end-pinching" is a rather plausible mechanism to explain the phenomenon. Figure 10 explains the ligament breakup process through this "end-pinching" mechanism. When a minimum neck diameter is reached in the ligament, Laplace pressure at this point increases due to reduction in local curvature of the neck. A nonuniform capillary pressure field propagates along the length of the ligament which subsequently creates a local flow reversal inside the ligament. This flow retracts the ligament in the reverse direction of the particle motion which eventually leads to pinch-off of the ligament by the action of surface tension force in attempt to minimize the ligament surface energy. We also note a similarity between this end-pinching phenomenon and the dripping mechanism for droplet breakup in microfluidics applications which occur due to interplay of three different forces—surface tension force, shear stress force, and the tip resistance force.[30,31] In a T type microchannel, Yang et al.[31] demonstrated three different droplet breakup mechanisms namely squeezing, dripping, and jetting using LBM simulations in the Capillary number range of 0.002–0.056. The important feature of the dripping mechanism is that droplet begins to necking with time and never touches the top wall of the microchannel until the neck snaps off. It was reasoned that the neck thinning step is induced by the shear stress of the continuous phase and also the pressure difference between the upstream and downstream sides of the droplet. We note the fact that transition from squeezing to dripping regime in their study was reported to occur when the Capillary number was increased to 0.01 which was also the observed threshold of capillary

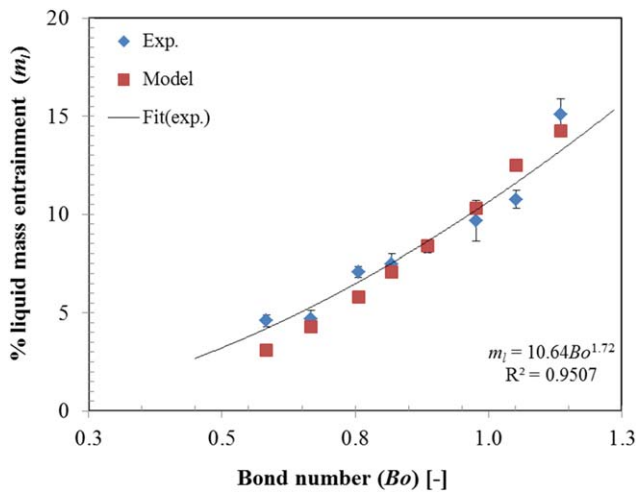

Figure 11. Comparison of liquid mass entrainment (% of film mass) predicted by the model with the experimental measurements.

[Color figure can be viewed in the online issue, which is available at wileyonlinelibrary.com.]

number in the present study above which the complete penetration involving ligament formation was always observed to occur.

Liquid mass entrainment

A certain liquid entrainment with particle was consistently observed at higher Weber number cases after ligament breakup. Experimentally measured % film mass entrainment (blue diamonds) is compared with energy balanced-based model prediction (red filled squares) in Figure 11. Model predicted liquid entrainment was found to vary from 3.1 to 15% of the liquid film mass which agreed reasonably well with the experimental measurement of 4.6–15% over the range of Bond number reported in Figure 11. An increasing trend of liquid mass entrainment can be noticed as particle diameter (Bond number) is increased. Intuitively, for a hydrophilic particle (contact angle $<90°$), more liquid adherence would be expected as the particle surface area increases which is confirmed by the model prediction. A good correlation between the %film mass entrainment and corresponding particle Bond number ($R^2 = 0.95$) was obtained which indicated a dependency of $Bo^{1.72}$. A value of 1.9 was obtained for multiplier K to compute the ligament breakup time (Eq. 19) by minimizing the sum of square errors between the model predictions and experimental data. The model predicted ligament breakup times were in the range of 6.1–12.3 ms over the Bond number range indicated in Figure 11 which agreed well with the experimentally observed average ligament breakup time of $\sim$7.9 ms. The model predicts 58–75% loss of initial particle kinetic energy corresponding to Bond numbers in Figure 11 which is spent toward this liquid mass entrainment.

It would be worthwhile to mention that in the proposed model of liquid entrainment (Eq. 21), the two unknown parameters—TPCL position and particle-ligament velocity, v_{pl} were simplified into a single parameter—particle-ligament velocity under the assumption of a no slip condition on particle surface and a constant cone angle during ligament breakup process. Recognizably, any discrepancy on the model outcome would result from this assumption of stationary contact line and additionally from the consideration of conical geometry of the ligament which actually takes shape of a cylindrical strand connected to a smaller cone at the time of detachment (Figure 9). Nonetheless, acknowledging the complexities involved in the ligament breakup process, this simplified model can be considered useful to have a theoretical estimation of the liquid mass entrainment and can be utilized for droplet-particle collision case with certain modifications.

Forces on particle

It is also interesting to understand the effect of various forces that govern the interaction outcomes. In CFD modeling, the contributions of all forces were lumped into pressure force (sum of static and dynamic pressure integrated over particle surface) and viscous force (shear stress integrated over particle surface). The viscous force arises primarily due to the liquid motion in the film imparted by particle during impact. Pressure force, on the other hand, comprises a static component due to hydrostatic heads of fluids and a dynamic component due to motion of liquid around the particle surface. These forces are presented in Figures 12a–f for three representative Weber number cases with different contact angle BCs.

In low Weber number case ($We = 1.4$, Figures 12a, b), viscous force acting on particle could be seen lower by an order of magnitude than the corresponding pressure force. Of all the BCs shown, magnitude of the forces computed by receding contact angle BC is found to be generally higher followed by static contact angle and advancing contact angle BC in the decreasing order. This trend can be attributed to the higher wetting characteristic at lower contact angle value which results in quicker submergence of the particle indicating a distinct peak in the force profile.

As Weber number is increased ($We = 11.7$, Figures 12c, d), clearly two distinct peaks in the force profiles could be noticed which correspond to resistance associated with penetration of the top and bottom interface, respectively. While the first peak invariably occurs due to receding contact angle BC leading to complete wetting, the second peak appears due to non-physical stretching of interface resulted from the use of advancing contact angle BC.

The dominance of pressure force over viscous force and the presence of peaks in force profile are also noticeable in the higher Weber number case ($We = 22.5$, Figures 12e, f). However, in later stages of interactions, the force magnitude predicted by the advancing contact angle BC indicates a steady decline which can be attributed to the early detachment of the particle from the connecting ligament. The force profiles for both static and receding contact angle BC indicate a rather flat trend implying stretching of the ligament attached to the particle which in contrast to the experimental observations does not lead to an expected breakup.

It is obvious that due to momentum transfer from particle to film, the gas pressure in the system especially in the confined space below bottom interface (Figure 3a, position B) would essentially change. However, in the proposed energy balance model for complete penetration case, any energy change associated with gas phase was ignored. Figures 13a–c presents temporal change of static pressure on bottom wall of capillary tube predicted by the CFD model with three different contact angle BCs for the three Weber number cases. In general, it could be noticed that as particle Weber number increases, fluctuation of static pressure on the base surface increases as well (peak fluctuating pressure is <100 Pa in *We*-1.4 case and $\sim$250 Pa in *We*-22.5 case). These pressure fluctuations are indeed more when particle passes through the film leading to significant interface deformation. Noticeably, the magnitude of fluctuations increases in all the cases particularly when the advancing contact angle BC is applied which could be explained by more distortion of the interface involving formation and breakup of the gas-cavity and associated interface shape change afterward. Toward the end of the interaction dynamics in almost all the cases and specifically in *We*-22.5 case where complete film penetration occurs, static pressure could be seen reaching the same initial magnitude of $\sim$ 30 Pa. The CFD model prediction therefore justifies the assumption of neglecting any gas-phase energy change in the energy balance model.

Conclusions

In the present work, particle interactions with a suspended stationary liquid film were studied at different impact velocities both experimentally and numerically. In accord to the stated aims of this study, the conclusions are summarized below.

Broadly two different types of particle-film interactions were observed namely retention/capture and complete penetration. These interactions outcomes were simulated by a VOF-based 3-D CFD model by performing a sensitivity analysis

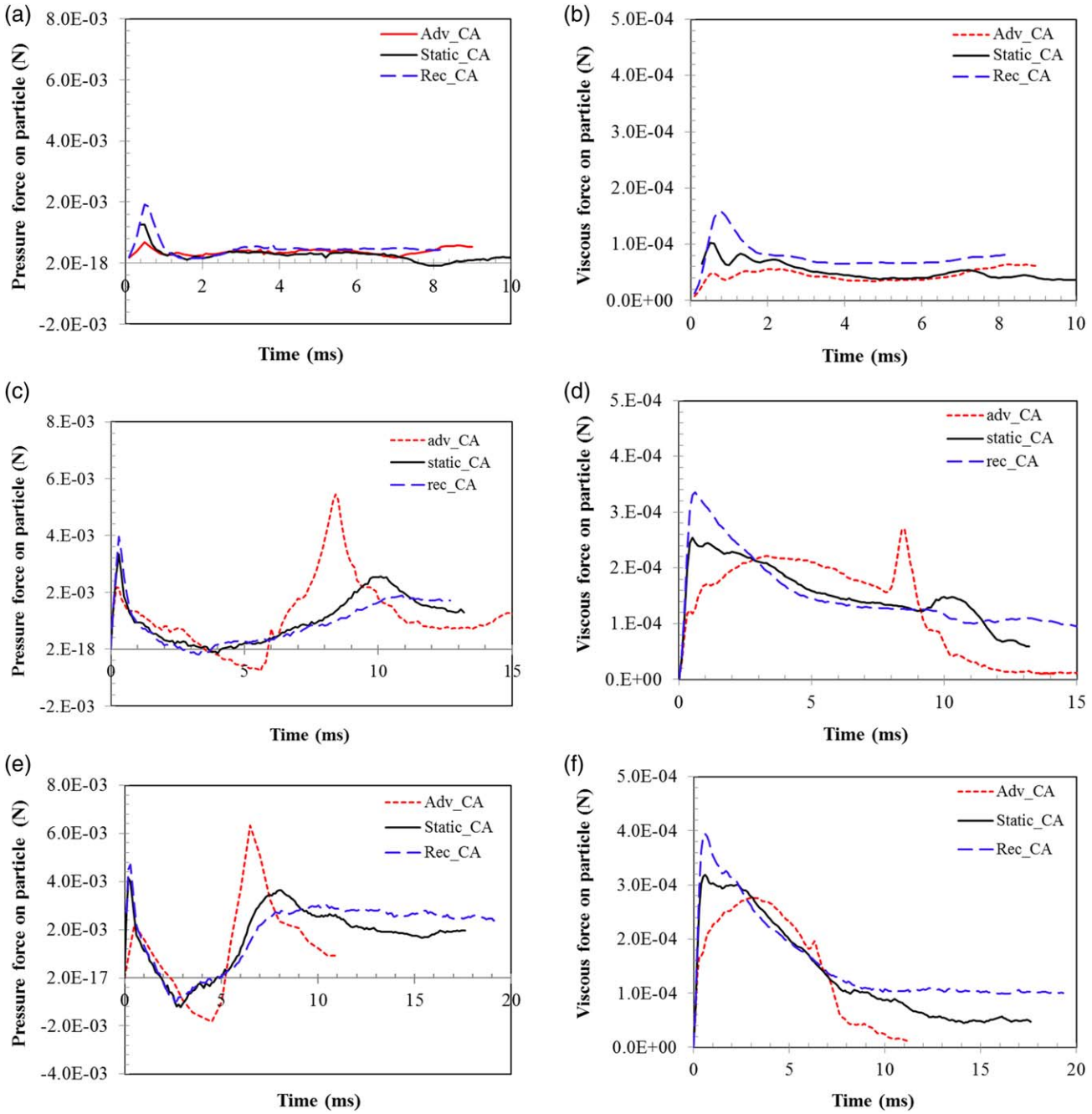

Figure 12. Comparison of pressure and viscous force magnitudes predicted by the CFD model ($d_p = 2.05$ mm) with advancing, θ_a; static, θ_s; and receding, θ_r contact angle boundary conditions showing (a) pressure force at $We = 1.4$, (b) viscous force at $We = 1.4$, (c) pressure force at $We = 11.7$, (d) viscous force at $We = 11.7$, (e) pressure force at $We = 22.5$, and (f) viscous force at $We = 22.5$ case.

In all these cases, pressure force remains higher than viscous force almost by an order of magnitude. [Color figure can be viewed in the online issue, which is available at wileyonlinelibrary.com.]

involving advancing, static and receding contact angle boundary conditions. The advancing contact angle BC reasonably captured the gas cavity formation at the top interface at intermediate ($We = 11.7$) to higher Weber number cases ($We = 22.5$) which could not be obtained when the static and receding angle BC were used. On the contrary, at the bottom interface, static and receding contact angle BC gave plausible predictions of ligament shape and particle velocity compared to the advancing contact angle BC scenario.

Although, in general the CFD model with some specific boundary conditions predicted the particle motion well especially within the film, few discrepancies were observed compared to experiments which can be attributed to the following reasons: (1) small nonsphericity of the particles used in the experiments contrary to perfect spherical shape assumed in the CFD model, (2) orientation, that is, flat face or sharp face of the particle pointing to film interface during impact, and (3) lack of a sound physical submodel in the CFD model that can account for contact angle variations during the entire interaction process.

An energy balance model was proposed to determine the fate of particle-film interactions introducing a collision

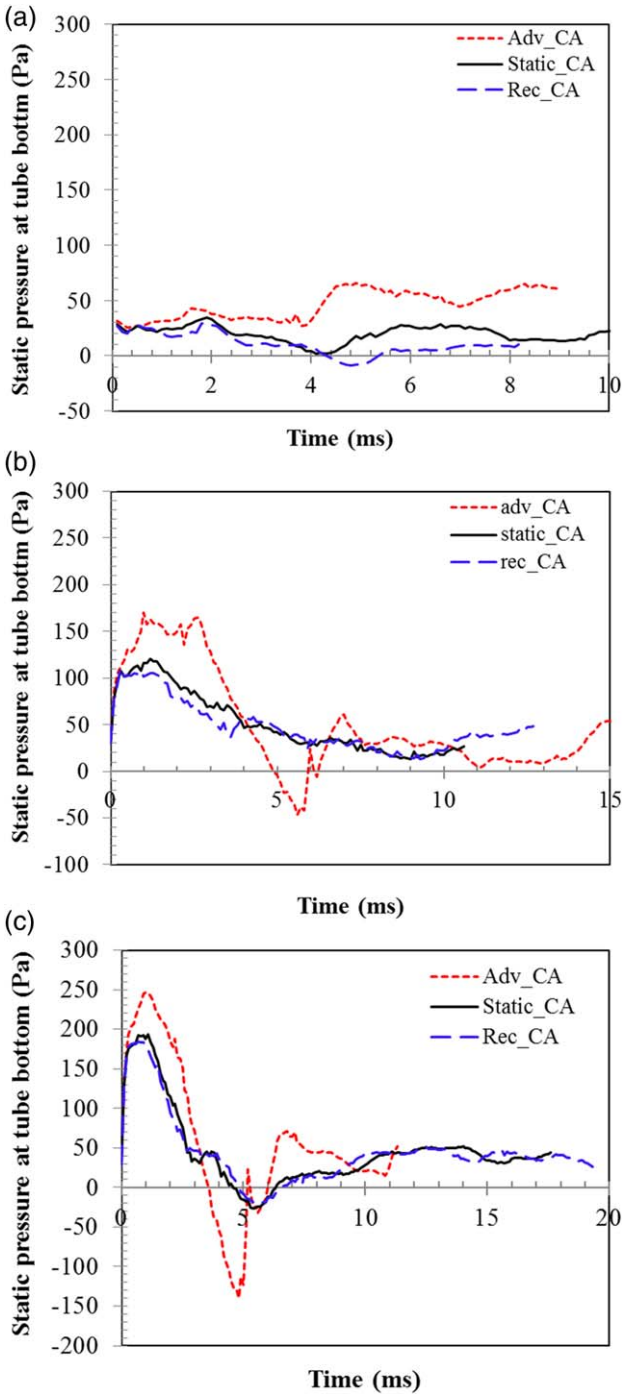

Figure 13. CFD model predictions of fluctuations of system static pressure at the bottom surface of capillary tube for three representative cases (a) *We*-1.4, (b) *We*-11.7, and (c) *We*-22.5.

Pressure fluctuations are relatively more at higher *We* number cases. In general, the static pressure remains almost constant around its initial value of ~30 Pa at the later stages of interactions. [Color figure can be viewed in the online issue, which is available at wileyonlinelibrary.com.]

parameter (C) which indicates particle retention at $C > 1$ and penetration at $C < 1$. The parameter was found to predict experimental outcomes quite reasonably excepting few cases near the transition point which could be attributed to the reasons stated earlier. The fitted trend of the collision parameter indicates a strong inverse relationship with the particle Weber number.

At complete penetration, a liquid ligament was observed to form which kept the particle connected to the bottom film interface. The breakup of this ligament was observed to occur at $We_{\mathrm{lig}} < 4$ without any visible capillary waves on the ligament interface. Present observations and previously reported analysis suggest that particle-induced ligament breakup occurs only through "dripping" or "end pinch-off" mechanism. A theoretical model based on the energy balance approach was suggested to predict the liquid mass entrainment with particle in the complete penetration case which agreed reasonably well with the experimental measurements (model predicted liquid entrainment: 3.1–14% of film mass against experimental measurements: 4.6–15% of film mass). Also, the attached liquid mass was observed to increase with particle diameter and showed a good correlation with Bond number as $Bo^{1.72}$.

The role of different forces in the particle-film interactions was analyzed using the CFD model which indicates that pressure force always remains higher than the viscous force almost by an order of magnitude. Presence of peaks in the force profiles relates to higher resistance encountered at the interface. Noticeably, use of receding contact angle BC leads to higher force magnitude due to higher wetting behavior while the use of advancing contact angle leads to a lower magnitude of force due to the dewetting behavior.

Further effort in this area is indeed required to implement a robust physical model for contact angle variation such as the one suggested by Shikhmurzaev[21,22] utilizing coupled VOF and IB approach to successfully model such complex interfacial interaction phenomena.

Acknowledgments

The authors gratefully acknowledge the financial support from Australian Research Council (ARC) and British Petroleum (BP), Kwinana, Western Australia to carry out this research work. Also, the critical comments of the reviewers to improve the work are sincerely acknowledged.

Literature Cited

1. Ge Y, Fan L-S. Droplet-particle collision dynamics with film boiling evaporation. *J Fluid Mech*. 2007;573:311–337.
2. Mitra S, Sathe MJ, Doroodchi E, Utikar R, Shah MK, Pareek V, Joshi JB, Evans GM. Droplet impact dynamics on a spherical particle. *Chem Eng Sci*. 2013;100:105–119.
3. Mitra S, Doroodchi E, Pareek V, Joshi JB, Evans GM. Collision behaviour of a smaller spherical particle on a larger stationary droplet. *Adv Powder Technol*. 2014;26(1):280–295.
4. Hoeven van der MJ. *Particle-Droplet Collisions in Spray Drying*. PhD Thesis. Australia: School of Engineering, University of Queensland, 2008.
5. Wu Y, Zhang J, Lavernia, EJ. Modelling of the incorporation of ceramic particulates in metallic droplets during spray atomization and co-injection. *Metall Mater Trans B*. 1994;25B:135–147.
6. Liu D, He Q, Evans GM. Penetration behaviour of individual hydrophilic particle at a gas-liquid interface. *Adv Powder Technol*. 2010; 21:401–411.
7. Vella D, Lee D-G, Kim H-Y. Sinking of horizontal cylinder. *Langmuir*. 2006;22:2972–2974.
8. Vella D, Lee D-G, Kim H-Y. The load supported by small floating objects. *Langmuir*. 2006;22:5979–5981.
9. Lee D-G, Kim H-Y. Impact of superhydrophobic sphere onto water. *Langmuir*. 2008;24:142–145.
10. Lee D-G, Kim H-Y. Sinking of small sphere at low Reynolds number through interface. *Phys Fluids*. 2011;23(072104):1–9.

11. Gac JM, Gradon L. Lattice-Boltzmann modelling of collisions between droplets and particles. *Colloids Surf A Physiochem Eng Asp*. 2014;441:831–836.
12. Dubrovsky VV, Podvysotsky AM, Shraiber AA. Particle interaction in three phase polydisperse flows. *Int J Multiphase Flow*. 1992; 18(3):337–352.
13. Nguyen AV, Schulze HJ. *Colloidal Science of Flotation*. Surfactant Series 118, Chapter 23. Marcel Dekker, New York, 2004:527–559.
14. Petrov PG, Petrov JG. A combined molecular-hydrodynamic approach to wetting kinetics. *Langmuir*. 1992;8:1762–1767.
15. Ozawa Y, Mori K. Critical condition for penetration of solid particle into liquid metal. *Trans ISIJ*. 1983;23:769–774.
16. Ito M, Sato T. In situ observation of a soap film catenoid-a simple educational physics experiment. *Eur J Phys*. 2010;31:357–365.
17. Hoeve van W, Gekle S, Snoeijer JH, Versluis M, Brenner MP, Lohse D. Breakup of diminutive Rayleigh jets. *Phys Fluids*. 2010; 22(122003):1–11.
18. Day RF, Hinch EJ, Lister JR. Self-similar pinch off of an inviscid fluid. *Phys Rev Lett*. 1998;80:704–707.
19. Castrejon-Pita JR, Castrejon-Pita AA, Hinch EJ, Lister JR, Hutchings IM. Self-similar breakup of near-inviscid fluids. *Phys Rev E*. 2012;86,15301(R):1–4.
20. Ansys FLUENT Theory Guide, Release 14, Chapter 1, 2011, Ansys Inc., Lebanon, NH, USA.
21. Shikhmurzaev YD. Dynamic contact angles and flow in vicinity of moving contact line. *AIChE J*. 1996;42(3):601–612.
22. Shikhmurzaev YD. The moving contact line on a smooth solid surface. *Int J Multiphase Flow*. 1993;19(4):589–610.
23. Sikalo S, Wilhelm H-D, Roisman IV, Jakirlic S, Tropea C. Dynamic contact angle of spreading droplets: experiments and simulations. *Phys Fluids*. 2005;17(062103):1–13.
24. Yokoi K, Vadillo D, Hinch J, Hutchings I. Numerical studies of the influence of the dynamic contact angle on a drop impacting on a dry surface. *Phys Fluids*. 2009;21(072102):1–12.
25. Deen NG, Annaland MVS, Kuipers JAM. Direct numerical simulation of complex multi-fluid flows using a combined immersed boundary (IB) and volume of fluid (VOF) approach. In: *Fifth International Conference on CFD in the Process Industries*. Melbourne, Australia: CSIRO, December 13–15, 2006.
26. Pougatch K, Salcudean M, McMillan J. Three-dimensional numerical modelling if interactions between a gas-liquid jet and a fluidized bed. *Chem Eng Sci*. 2012;68:258–277.
27. Stone HA, Bentley BJ, Leal LG. An experimental study of transient effects in the breakup of viscous drops. *J Fluid Mech*. 1986;173:131–158.
28. Webster DR, Longmire EK. Jet pinch-off and drop formation in immiscible liquid-liquid systems. *Exp Fluids*. 2001;30:47–56.
29. Zhang X, Basaran OA. An experimental study of dynamics of drop formation. *Phys Fluids*. 1995;7(6):1184–1203.
30. Garstecki P, Fuerstman MJ, Stone HA, Whitesides GM. Formation of droplets and bubbles in a microfluidic T-junction-scaling and mechanism of breakup. *Lab Chip*. 2006;6:437–446.
31. Yang H, Zhou Q, Fan L-S. Three dimensional numerical study on droplet formation and cell encapsulation process in a micro T-junction. *Chem Eng Sci*. 2013;87:100–110.

Appendix

Figure A1 presents the interface profile of the gas cavity which can be defined by a catenary curve

$$r(y)=r_{\mathrm{cav,c}}\cosh\left(\frac{y}{r_{\mathrm{cav,c}}}\right) \tag{A1}$$

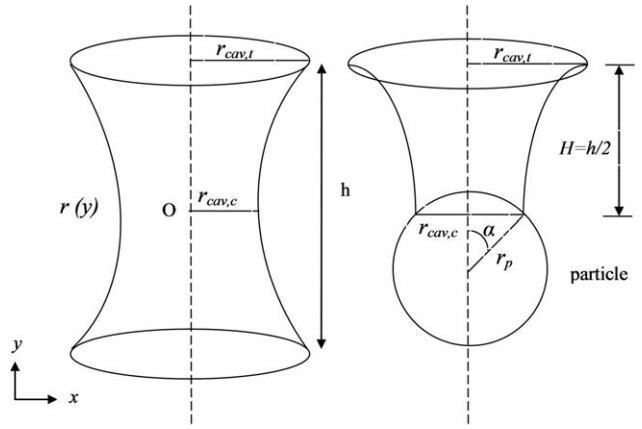

Figure A1. Schematic of the interface profile described by a catenoid geometry.

The catenoid is produced by rotating the catenary curve around the axis of symmetry (y) where $r_{\mathrm{cav},t}$ is radius of top ring, $r_{\mathrm{cav,c}}$ is radius of central ring and H is height of interface depression. $r_{\mathrm{cav,c}}$ can be substituted by radius of three phase contact perimeter r_{tpcl} as $r_{\mathrm{tpcl}}=r_{\mathrm{p}}\sin\alpha$.

The interface depression height H ($=h/2$) can be related to radius of center ring, $r_{\mathrm{cav,c}}$ and radius of top ring $r_{\mathrm{cav},t}$ using Eq. A1 noting that at $y=h/2$, $r=r_{\mathrm{cav},t}$,

$$r_{\mathrm{cav},t}=r_{\mathrm{cav,c}}\cosh\left(\frac{h}{2r_{\mathrm{cav,c}}}\right) \tag{A2}$$

The surface area of gas cavity is half of surface area of the complete catenoid and is derived as follows

$$S_{\mathrm{cavity}}=\frac{1}{2}\left[2\pi\int_0^{h/2} r(y)\sqrt{1+\left(\frac{dr(y)}{dy}\right)^2}\,dy\right]. \tag{A3}$$

Equation A3 can be simplified with help of Eq. A2 to obtain final expression of the cavity surface area as

$$\begin{aligned}S_{\mathrm{cavity}}&=\pi\int_0^{h/2} r_{\mathrm{cav,c}}\cosh\left(\frac{y}{r_{\mathrm{cav,c}}}\right)\sqrt{1+\sinh^2\left(\frac{y}{r_{\mathrm{cav,c}}}\right)}\,dy\\&=\frac{\pi r_{\mathrm{cav,c}}}{2}\int_0^{h/2}1+\cosh\left(\frac{2y}{r_{\mathrm{cav,c}}}\right)dy\\&=\pi r_{\mathrm{cav,c}}^2\left[\cosh^{-1}\left(\frac{r_{\mathrm{cav},t}}{r_{\mathrm{cav,c}}}\right)+\frac{1}{2}\sinh\left(2\cosh^{-1}\left(\frac{r_{\mathrm{cav},t}}{r_{\mathrm{cav,c}}}\right)\right)\right].\end{aligned} \tag{A4}$$

Manuscript received Feb. 8, 2015, and revision received July 7, 2015.